PNAS

Supporting Information for

Cryosectioning-enhanced super-resolution microscopy for single-protein imaging across cells and tissues

Johannes Stein[1,2,*], Maria Ericsson[3], Michel Nofal[1], Lorenzo Magni[1], Sarah Aufmkolk[2], Ryan B. McMillan[1], Laura Breimann[2], Conor P. Herlihy[2], S. Dean Lee[2], Andréa Willemin[4,5], Jens Wohlmann[6], Laura Arguedas-Jimenez[4], Peng Yin[1], Ana Pombo[4,5], George M. Church[1,2,*] and Chao-ting Wu[2,*]

Corresponding authors: Johannes Stein, George M. Church, Chao-ting Wu
Email: johannes.stein@wyss.harvard.edu, gchurch@genetics.med.harvard.edu, twu@genetics.med.harvard.edu

This PDF file includes:

Supporting Information Text

Material and Methods

Materials. Unmodified, dye-labeled, and modified DNA oligonucleotides were purchased from Integrated DNA Technologies, Metabion and Biomers. Unmodified oligos were purified via standard desalting and modified oligos via HPLC. DNA scaffold strands were purchased from Tilibit (p7249, identical to M13mp18). Sample chambers were ordered from Ibidi GmbH (8-well 80827 and 18-well 81817). Tris 1M pH 8.0 (AM9856), EDTA 0.5M pH 8.0 (AM9261), Magnesium 1M (AM9530G) and Sodium Chloride 5M (AM9759) were ordered from Ambion. Streptavidin (S-888) Ultrapure water (15568025), PBS (20012050), 4',6-Diamidino-2-Phenylindole, Dihydrochloride (D1306) (A39255), BSA (AM2616) and TetraSpeck™ Microspheres 0.1 µm (T7279), DMEM (10569) and Dithiothreitol (DTT) were purchased from Thermo Fisher Scientific. BSA-Biotin (A8549), Tween-20 (P9416-50ML), Glycerol (cat. 65516-500ml), (+-)-6-Hydroxy-2,5,7,8-tetra-methylchromane-2-carboxylic acid (Trolox) (238813-5G), methanol (32213-2.5L), 3,4-dihydroxybenzoic acid (PCA) (37580-25G-F), protocatechuate 3,4-dioxygenase pseudomonas (PCD) (P8279-25UN), cell scrapers (CLS353085), Triton-X 100 (93443), Gelatin from cold fish skin (G7041-500G), Formamide (F9037), RNAse A (EN0531), Sodium Azide (S2002), HEPES (H4034-100G), FastAP Alkaline Phosphatase (EF0651), Methyl cellulose 25 CP (M6385-100G), Glycine (G8898), Sodium hydroxide (P3911-1kg), methyl cellulose (M6385), dextran sulfate (D4911), 20xSSC buffer (S6639), and sucrose (S0389) was purchased from Sigma-Aldrich. 10% fetal bovine serum was purchased from Genesee Scientific (25-514). EM grade paraformaldehyde (PFA) was purchased from Electron Microscopy Services (15714). 90 nm gold nanoparticles (G-90-20-10 OD10) were purchased from Cytodiagnostics. Primary anti-Lamin A/C (mouse, 34698), anti-LAMP1 (rabbit, 9091BF) and anti a-tubulin (rabbit, 2125BF) antibodies were purchased from Cell Signaling (mouse, 34698). Primary anti-Pol II CTD S5p (rabbit, ab5131), anti-Digoxigenin (mouse, ab420) and anti-SC35 (mouse, ab11826) antibodies were purchased from Abcam. Primary anti-Pol II CTD (mouse, CTD4H8) antibody was purchased from BioLegend. Secondary donkey anti-rabbit antibody labeled with Alexa488 was purchased from Thermo Fisher Scientific (A21206). Secondary donkey anti-mouse antibody labeled with Alexa647 was purchased from Jackson Immuno (715-605-150). Unconjugated secondary donkey anti-rabbit and (711-005-152) and goat anti-mouse (115-005-003) antibodies were purchased from Jackson ImmunoResearch Laboratories. DBCO-modified single domain antibodies against mouse IgG (N2005-DBCO) and rabbit IgG (N2405-DBCO) as well as mouse IgG multiplexing blocker(K0102-50) were purchased from NanoTag. 0.5-mL Amino Ultra Centrifugal Filters with 50 kDa and 10 kDa molecular weight cutoffs were purchased from Millipore (UFC5050 and UFC5010, respectively). DBCO-sulfo-NHS ester cross-linker was purchased from Vector Laboratories (CCT-A124). Qubit Protein Assay (Q33211), NuPage 4-12% Bis-Tris protein gels (NP0323BOX), NuPage LDS Sample Buffer (NP0007) was purchased from Invitrogen. InstantBlue Coomassie Protein Stain was purchased from Abcam (ab119211).

Buffers. Four buffers were used for sample preparation and imaging: Buffer A (10 mM Tris-HCl pH 7.5, 100 mM NaCl); Buffer B (5 mM Tris-HCl pH 8.0, 10 mM MgCl2, 1 mM EDTA); Buffer C (1× PBS, 500 mM NaCl); 10x folding buffer (100 mM Tris,10 mM EDTA pH 8.0, 125 mM MgCl2). Antibody storage buffer: 1%
BSA, 0.1% Sodium Azide, 10 mM EDTA, 50% glycerol). Buffers were checked for pH. Imaging buffers were supplemented with oxygen scavenging & triplet state quenching system 1× PCA, 1× PCD, 1× Trolox prior to imaging.

PCA, PCD, Trolox. 100× Trolox: 100 mg Trolox, 430 µL 100% Methanol, 345 µL 1 M NaOH in 3.2 mL H2O. 40× PCA: 154 mg PCA was mixed with 10 mL water adjusted to pH 9.0 with NaOH. 100× PCD: 9.3 mg PCD, 13.3 mL of buffer (100 mM Tris-HCl pH 8, 50 mM KCl, 1 mM EDTA, 50% glycerol).

DNA origami design and assembly. DNA origami with 20-nm spaced docking strands ('20 nm grids') were designed previously using the Picasso Design (1) module. A list of all used DNA

strands can be found in ref. (2). Folding of structures was performed using the following components: single-stranded DNA scaffold (0.01 µM), core staples (0.1 µM), biotin staples (0.01 µM), extended staples for DNA-PAINT (each 1 µM), 1x folding buffer in a total of 50 µl for each sample. Annealing was done by cooling the mixture from 80 °C to 25 °C in 3 hours in a thermocycler. Using a 1:1 ratio between scaffold and biotin staples allows sample preparation without prior DNA origami purification, where otherwise free biotinylated staples would saturate the streptavidin surface and prevent origami immobilization on the glass surface. As docking strand sequence, we used a 20nt adapter motif (3) (A20: AAGAAAGAAAAGAAGAAAAG), which allowed us to later hybridize any desired docking strand imaging to the origami via a stably-binding complementary adapter 'cA20_DS'. The adapter motif is cA20: CTTTTCTTCTTTTCTTTCTT which is concatenated to the docking strand of choice DS (see **Table S2** for sequences).

DNA origami sample preparation. Ibidi 8-well slides were prepared as follows. A 10 µl drop of biotin-labeled bovine albumin (1 mg/ml, dissolved in buffer A) was placed at the chamber center and incubated for 2 min and aspirated. The chamber was then washed with 200 µl of buffer A, aspirated, and then a 10 µl drop streptavidin (0.5 mg/ml, dissolved in buffer A) was placed at the chamber center and incubated for 2 min. After aspirating and washing with 200 µl of buffer A and subsequently with 200 µl of buffer B, a 10 µl of DNA origami (1:100-200 dilution in buffer B from folded stock) was placed at the chamber center and incubated for 5 min. Next, the chamber was washed with 200 µl of Buffer B and docking strand adapters hybridizing to the DNA origami were added at 100 nM in Buffer B, incubated for 5 min and washed with 200 µl Buffer B. Finally, Buffer C and imager strand was added for DNA-PAINT imaging.

Conjugation of secondary antibodies/nanobodies with docking strands. DNA antibody conjugations were performed in 0.5-mL Amino Ultra Centrifugal Filters with 50 kDa molecular weight cutoffs with DBCO-sulfo-NHS ester cross-linker, which was dissolved at 20 mM DMSO and stored in single-use aliquots at -80° C. This cross-linker links azide-functionalized DNA oligonucleotides to surface-exposed lysine residues. Azide-functionalized DNA oligonucleotides were stored at 1 mM in deionized water. Critically, all antibodies were ordered carrier-free, as common preservatives such as bovine serum albumin and sodium azide interfere with the conjugation reaction. First, 500 µL PBS was added to the Amicon filters, which were centrifuged for 5 min at 10,000 rcf. After wetting the filters, 25 µg antibody was added and washed twice with PBS. For each wash, PBS was added to a total volume of 500 µL, and the filters were centrifuged for 5 min at 10,000 rcf. If after the second spin, the total volume remaining in each filter was greater than 100 µL, the filters were centrifuged again for 5 min at 10,000 rcf. After the second PBS wash, a 20-fold molar excess of DBCO-sulfo-NHS ester cross-linker and a 20-fold molar excess of DNA oligonucleotide were added, and after gentle mixing, each conjugation reaction was incubated in the dark at 4° C overnight. The following day, conjugated antibodies were washed three times with PBS, as described above. To elute the antibody, the filter was inverted in a fresh tube and centrifuged for 2 min at 1,500 rcf. The conjugated antibody was transferred to a clean tube and stored at -20° C in antibody storage buffer. Concentrations were measured using the Qubit Protein Assay. DNA-antibody conjugation was confirmed by comparing unconjugated and conjugated antibodies on NuPage 4-12% Bis-Tris protein gels. For each sample, 0.5 µg total protein was added to NuPage LDS Sample Buffer and 50 mM DTT. Protein was denatured at 80° C for 10 min. Gels were run at 75 V for 5 min, then at 180 V for 60 min. Gels were stained with InstantBlue Coomassie Protein Stain for 15 minutes at room temperature, rinsed with water, and imaged on a Sapphire Biomolecular Imager (Azure Biosystems).
Conjugation of DBCO-modified nanobodies (also "single domain antibody") was performed analogously, but in 0.5-mL Amino Ultra Centrifugal Filters with 10 kDa molecular weight cutoffs. After filter wetting and washing, 25 µg nanobody was added and washed twice. For each wash, PBS was added to a total volume of 500 µL, and the filters were centrifuged for 5 min at 10,000 rcf. After the second PBS wash, a 5-fold molar excess of DNA oligonucleotide were added, and after gentle mixing, each conjugation reaction was incubated in the dark at 4° C overnight. The next day, conjugated nanobodies were washed three times and transferred to a clean tube for storage at -20° C in antibody storage buffer. Concentrations were measured using the Qubit Protein Assay

and working aliquots were adjusted to 5 mM in antibody storage buffer as recommended by the manufacturer.

Tissues. Mouse tissue was obtained from naïve control mice meeting experimental endpoint on an approved Harvard Medical School/Longwood Medical Area IACUC protocol.

Cell culture and plating. HeLa cells were maintained in DMEM supplemented with 10% fetal bovine serum at 37 °C with 5% CO2 and were checked regularly for mycoplasma contamination. For imaging of whole HeLa cells, ~16K cells were seeded in each well of an Ibidi 18-well chamber, placed in the incubator overnight and fixed the following day. For preparation of cell pellets for cryosectioning, ~1 million cells were seeded in 10-cm dishes and placed in the incubator until reaching 70 % confluency.

HeLa cell preparation for cryosectioning. HeLa cells were processed according to previously published protocols (4). In brief, HeLa cells were grown in 10 cm Petri dishes and once reaching 70 % confluence, were fixed in 4% PFA 250 mM HEPES, pH 7.6 for 10 min. Fixative was decanted and cells further fixed with 8% PFA in 250 mM HEPES, pH 7.6 for a total of 2h at 4°C. During fixation, cells were gently scraped off the surface unidirectionally using cell scrapers previously soaked in fixative to avoid sticking. Detached cell suspension was transferred into a 1.5 mL hydrophobic Eppendorf tube and centrifuged at increasing speeds to form a pellet of fixed cells: 300 × g, 5 min; 500 × g, 2 min; 1,000 × g, 2 min; 2,000 × g, 2 min; 4,000 × g. At this point, the pellet could be resuspended in 1% PFA in 250 mM HEPES, pH 7.6 and stored overnight at 4°C. Next, the pellet was transferred between several drops of 2.1 M sucrose drops to wash away residual fixative and infiltrated 2-4h in 2.1 M sucrose (sucrose acts as cryoprotectant to prevent structural damage during freezing. The pellet becomes transparent). Next, the infiltrated pellet was transferred to a metal pin, residual sucrose carefully removed using filter paper and the pellet shaped into a cone under a dissecting light microscope and using forceps. Finally, the cell pellet was frozen by immersion into liquid nitrogen and was stored indefinitely in liquid nitrogen tanks. We would like to also highlight alternative protocols based on gelatin embedding, which can improve probe handling as discussed in a recent review (5).

Tissue preparation for cryosectioning. Mouse cerebellum and spleen were sectioned into 1-2 mm cubes and incubated consecutively in 4% PFA 250 mM HEPES, pH 7.6, in 8% PFA in HEPES for 2 hours at 4°C, and in 1% PFA in HEPES overnight at 4°C. Tissue cubes were then embedded in 7.5% gelatin, 10% Sucrose in PBS (gelatin-sucrose solution was prepared at 70°C and stored in 10mL aliquots at -20°C). Tissues were infiltrated in liquid gelatin-sucrose for 30 minutes at 37°C and subsequently solidified at 4°C. Then, the gel block was removed from the tube, the tissue block cut out as 1mm blocks and transferred into 2.1 M sucrose in PBS for 4h. Lastly, sucrose-infiltrated tissue blocks were placed on metal pins, residual sucrose carefully removed using filter paper, frozen by immersion into liquid nitrogen and stored indefinitely in liquid nitrogen tanks.

Tokuyasu cryosectioning. All Tokuyasu cryosectioning was performed at the Harvard Electron Microscopy Core using a Leica EM UC7 Ultramicrotome equipped with a FC7 cryo-chamber. Frozen cell/tissue samples were cut at a temperature of -110°C using a diamond knife (Diatome). Lastly, sections were collected using drops of a freshly prepared 1:1 mixture of 2.1 M sucrose in PBS and 2% methyl cellulose in water and transferred onto Ibidi 8-well chambers for tkPAINT imaging, that had previously been glow discharged (EMS100x, 2min at 40mA). Sectioned samples can be stored at -20°C for months.

TEM imaging of Tokuyasu sections. For transmission electron microscopy imaging, cryosections were placed on formvar-coated grids, washed, and contrasted using methyl cellulose/uranyl acetate. TEM imaging was performed at the Harvard Electron Microscopy Core on a JEOL 1200EX TEM.

HeLa cell fixation, epon embedding and sectioning for TEM imaging

HeLa cells were grown in 10 cm Petri dishes and once reaching 70 % confluence, were fixed in 4% PFA 250 mM HEPES, pH 7.6 for 15 min followed by three washes in PBS for 2 min each. For permeabilized samples, permeabilization was applied in Petri dish, followed by three washes in PBS. Cells were gently scraped and collected into a 0.5 mL tube and centrifuged at 200 × g for two min to form pellets. The solution was exchanged and pellets stored in 1% PFA in 250 mM HEPES, pH 7.6 overnight at 4 °C. The next day, cell pellets were postfixed with 1% Osmium Tetroxide (OsO4)/1.5% Potassium Ferrocyanide(KFeCN6) for 1 hour, washed 2× in water, 1× Maleate buffer (MB) 1× and incubated in 1 % uranyl acetate in MB for 1 hr followed by 2 washes in water and subsequent dehydration in grades of alcohol (10 min each; 50%, 70%, 90%, 2×10min 100%). The samples were then put in propylene oxide for 1 h and infiltrated ON in a 1:1 mixture of propylene oxide and TAAB Epon (TAAB Laboratories Equipment Ltd, https://taab.co.uk). The following day the samples were embedded in TAAB Epon and polymerized at 60 °C for 48 h. Ultrathin sections (~80 nm) were cut on a Reichert Ultracut-S microtome, picked up onto copper grids, stained with lead citrate and examined in a Tecnai Spirit BioTwin Transmission electron microscope. Images were recorded with an AMT NanoSprint43-MkII camera.

Immunogold TEM imaging
Tokuyasu sectioning was performed at -120 °C and at ~80 nm cryosection thickness. Sections were picked up on a drop of 2.3 M sucrose with a small amount of 2% methyl cellulose added (9:1 mixture) and transferred to formvar-carbon coated copper grids. Gold labeling was carried out at room temperature on a piece of parafilm: antibodies were diluted in 1% BSA in PBS Grids, floated on drops of 1% BSA for 10 minutes to block for unspecific labeling, transferred to 5 µl drops of primary antibody and incubated for 30 minutes. Subsequently, grids were washed in 4 drops of PBS (total 10 min) before incubation in 10nm Protein A-gold (University Medical Center, Utrecht, the Netherlands) for 20 min. Grids were washed in 2 drops of PBS followed by 4 drops of water (total 15 min). The labeled sections were contrasted and embedded in methyl cellulose by floating the grids on a mixture of 0.3% uranyl acetate in 2% methyl cellulose for 5 minutes before blotting excess liquid off on a filter paper. Grids were imaged on a JEOL 1200EX Transmission electron microscope and an AMT 2k CCD camera.

Labeling of cryosections for tkPAINT. 8-well chambers containing cryosections were thawed and washed 3× in PBS under agitation for 10min for sucrose removal and quenched with 100mM glycine in 100mM HEPES for 15min. Next, cryosections were permeabilized in 0.3% Triton-X 100 in PBS for 5min, rinsed 3× in PBS and ready for subsequent labeling. Note, that Tokuyasu immunogold protocols vary regarding antibody incubation times. A general rule of thumb is using high antibody concentrations and short incubation times, rather than low concentrations for extended incubations (6). Hence, we chose relatively high antibody dilutions (1:50-200) and could even observe strong antibody signal for incubations as short as 5min. For a systematic investigation, antibody titration series can be advised. For our proof-of-concept study we applied varying blocking and/or labeling conditions, which are listed in **Table S1** for all experiments with respect to blocking buffer as well as both antibody dilution and incubation times. The blocking buffer was used for both antibody/nanobody incubations and as a washing solution in between labeling in case of indirect primary and secondary antibody/nanobody labeling. After antibody labeling, cryosections were washed 3× in PBS, stained with 30 nM DAPI in PBS for 3min and washed again with PBS. For all tkPAINT experiments based on secondary nanobodies the samples were postfixed in 4% PFA for 5 min, followed by three washes in PBS prior to imaging and DAPI staining. Lastly, Buffer C and imager was added for tkPAINT imaging. Note that DAPI staining could fade for several rounds of washing, especially for Exchange-PAINT experiments. However, staining could be simply recovered by performing another round of DAPI staining at the same concentration as stated above.
Phosphatase control (Fig. 2c). Two cryosection samples were processed as previously described until the blocking step, at which they were placed for 1h at 37°C and one incubating with alkaline phosphatase to remove phosphorylation site S5p as target antigen (4). After washing 3× in PBS, normal blocking and indirect immunostaining was performed using a fluorescently-labeled secondary antibody.
Combined a-tubulin and telomere imaging (Fig. 4c). Cryosections were labeled for a-tubulin using

primary antibody + secondary antibody incubation and postfixed with 4% PFA in PBS for 10min followed by a 10min glycine quenching step. Next, the samples were washed with PBS, and incubated with 100-fold diluted RNase A/T1 Mix in 1× PBS at 37 °C for 1 h. Samples were washed 3× in PBS, rinsed and incubated with 50% formamide in 2× SSC for 15min. Next, the sample was placed on a heat block at 90 °C for 4.5 min in 50% formamide in 2× SSC. A 20nt FISH probe against telomeric repeat (AACCCTAACCCTAACCCTAA
-A488) was added at 1 µm concentration in 20% formamide, 10% dextran sulfate and 4× SSC and incubated overnight at 37°C for hybridization. Lastly, the sample was washed 2× with 20% formamide 2× SSC, rinsed with PBS, and 30 nM DAPI in PBS for 3min was added. After a final wash in PBS, Buffer C was added and imager for tkPAINT imaging. *mRNA imaging via poly(dT) probes (Fig. 4d)*. Cryosections were treated as described until the blocking step, followed by a 10min wash in 4x SSC. Next, 40nt poly(dT) probe modified with digoxigenin were added in 20% hybridization buffer (20% ethylene carbonate, 10% dextran sulfate and 4× SSC) buffer at 37 °C overnight in a humidity chamber. The next day, the sample was washed 2× with 20% EC 2xSSCT for 15min, followed by three rinses with 4× SSC. The sample was then blocked with 1% gelatin in PBS for 10min and subsequently subject to indirect immunostaining as described in **Table S1**. After final washes, Buffer C and imager was added for tkPAINT imaging.

Fixation and labeling for whole HeLa cell imaging. 24h after seeding HeLa cells in Ibidi 18-well chambers, cells were fixed using 4% PFA 250 mM HEPES, pH 7.6 for 20min. Next, samples were washed 4× in PBS (30s, 60s, 2×5 min) and both blocked and permeabilized in 3% BSA and 0.25% Triton X-100 in PBS at room temperature for 90 min. Primary rabbit anti-Pol II S5p antibody was added at 1:100 in 3% BSA and 0.1% Triton-X 100 in PBS and incubated overnight at 4 °C. The next morning, samples were washed 4x washes in PBS (30s, 60s, 2× 5min) and DNA-conjugated secondary antibody (1:100) was added at 1:100 in 3% BSA and 0.1% Triton-X 100 in PBS and incubated for 1h at room temperature. Samples were quickly washed 3× in PBS, incubated with gold particles as fiducial markers (1:20 in PBS) for 5 min, washed again 2× in PBS before adding Buffer C and imager for DNA-PAINT imaging. For diffraction-limited immunofluorescence microscopy in Fig. S14 immunolabeling was performed as above using primary antibodies (mouse SC35 and rabbit Pol II S5p) and the respective dye-conjugated secondary antibodies (1:1000).

Super-resolution microscopy setup. TIRF and HILO imaging was carried out at MicRoN Imaging Core at Harvard Medical School on a Nikon Ti inverted microscope equipped with a Nikon Ti-TIRF-EM Motorized Illuminator, a Nikon LUN-F Laser Launch with single fiber output (488nm, 90mW;561 nm, 70mW; 640nm, 65mW) and a Lumencore SpectraX LED Illumination unit. The objective-type TIRF system with an oil-immersion objective (Apo TIRF 100×/1.49 DIC N2). DNA-PAINT experiments were performed using the 560 nm laser line and fluorescence emission was passed through a Chroma ZT 405/488/561/640 multi-band pass dichroic mirror mounted on a Nikon TIRF filter cube located in the filter cube turret and a Chroma ET 595/50m band pass emission filter located on a Sutter emission filter wheel within the infinity space of the stand before image recording on a line on a sCMOS camera (Andor, Zyla 4.2) mounted to a standard Nikon camera port. For astigmatism-based 3D imaging, the C-mount side port of the microscope body was replaced by a custom-built construction allowing to insert a cylindrical lens in front of the camera (description including component list in **Fig. S17**).

Imaging conditions. All fluorescence microscopy data was recorded with the sCMOS camera (2048 × 2048 pixels, pixel size: 6.5 µm). Both microscope and camera were operated with the Nikon Elements software at 2×2 binning and cropped to the center 512 × 512 pixel field-of-view. The camera read out rate was set to 200 MHz and the dynamic range to 16 bit. For detailed imaging parameters specific to the data presented in all main and supplementary figures refer to **Table S1**.

Image analysis. Please refer to **Fig. S2** and **Fig. S8** for a detailed step-by-step illustration through all processing steps of super-resolution reconstruction. All DNA-PAINT/tkPAINT imaging data was processed and reconstructed using the Picasso (1) software suite, Fiji (7, 8) and previously-published (3, 9) and custom Python modules.

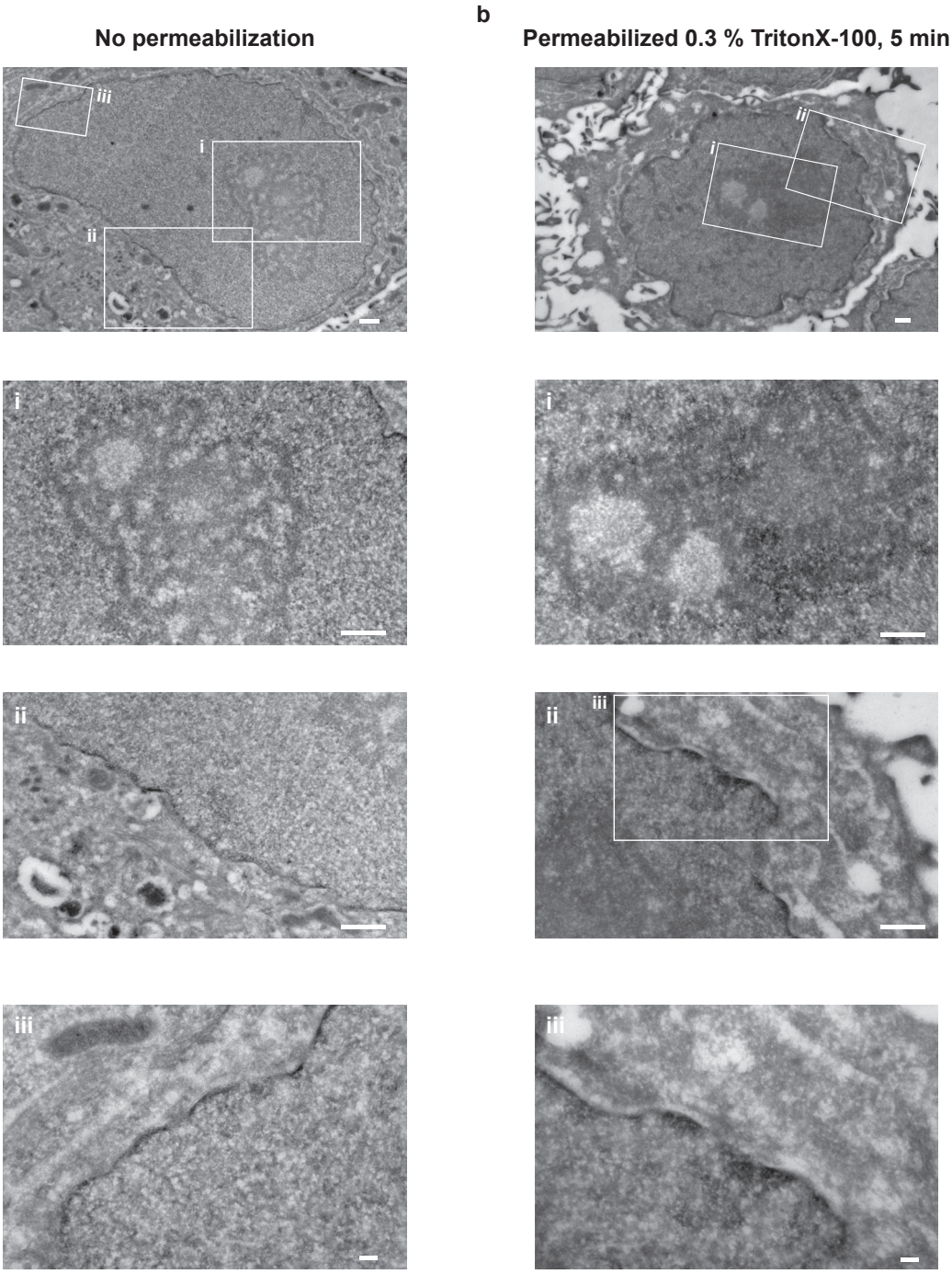

Fig. S1. TEM imaging confirms nuclear preservation in permeabilized cryosections. a Transmission electron microscopy (TEM) images of untreated 150 nm HeLa cryosections. Although ultrastructural studies are commonly performed in thinner cryosection (<100 nm), the contrast is sufficient to reveal structural features within the nucleus (nucleolus, nuclear envelope, and nuclear pores) and in the cytoplasm (endoplasmic reticulum, mitochondria, and cristae). The bottom three images show magnified regions of the same cell shown in the top image. **b** TEM images of 150 nm cryosections that were permeabilized with 0.3 % TritonX-100 for 5 min. As expected, detergent treatment affects lipids and membrane structures and results in observable extraction especially from the cytoplasmic domain. Overall, the intranuclear space, chromatin as well as the nucleolus appear ultrastructurally preserved. The bottom three images show magnified regions of the same cell shown in the top image. Scale bars, 500 nm, except 100 nm in (**a**iii and **b**iii).

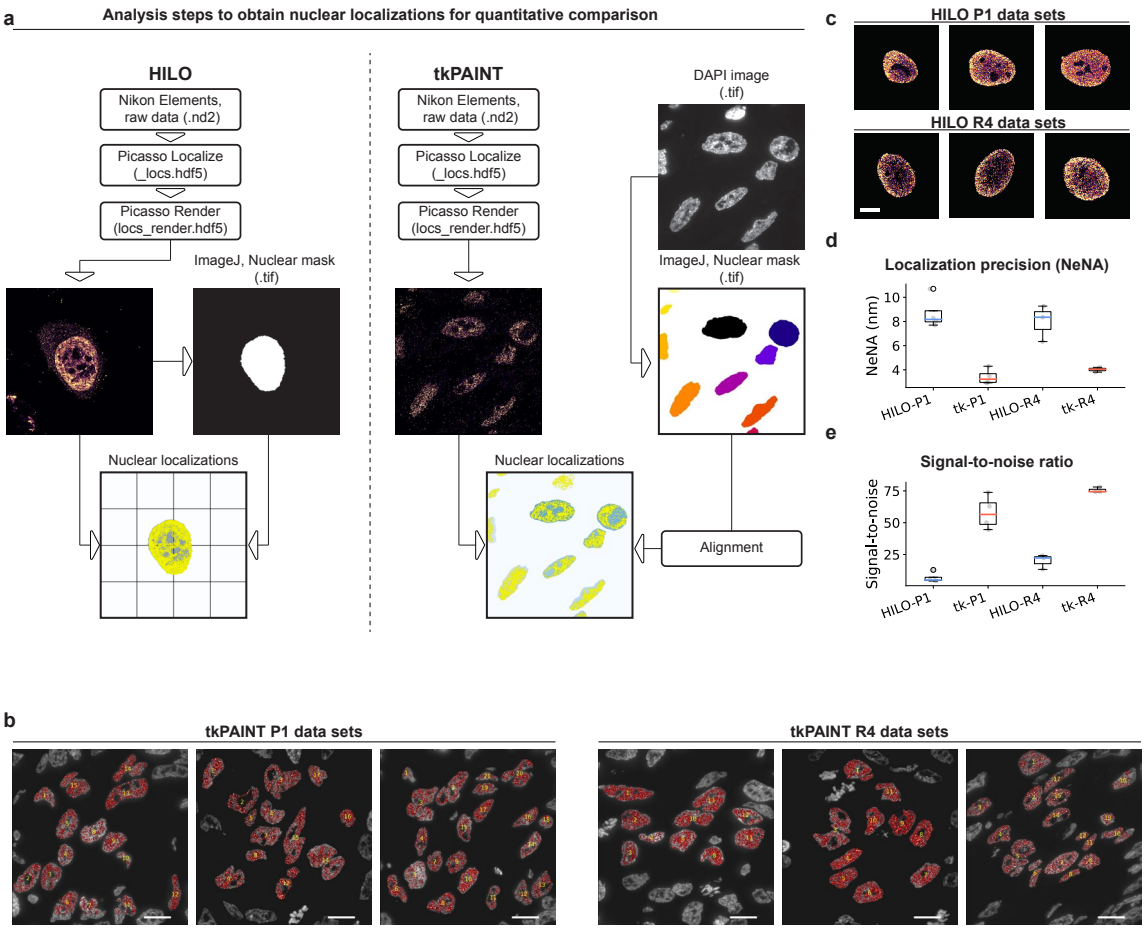

Fig. S2. Segmentation of nuclear localizations for quantitative comparison of HILO and tkPAINT. a Left: Workflow for nuclear segmentation in HILO DNA-PAINT imaging. Raw time series were recorded using Nikon Elements and processed with Picasso Localize software module (1). The localization files were subsequently loaded into Picasso Render (1) to perform drift correction (global correction via redundant-cross correlation (10) and subsequent correction based on gold particles as fiducials) and saved. From Picasso Render we further exported a low-resolution and oversaturated image, that we used to create a nuclear mask via FIJI (7) (thresholding to create a mask & the plugin BIOP/Image Analysis/ROIs/ ROIs to label image to export a binary mask as .tif file. https://github.com/BIOP). Using a custom Python script, both the drift corrected localization file and the binary mask were loaded to filter for nuclear localizations based on the mask. Note: we did not use DAPI staining for nuclear segmentation as in tkPAINT due to poor image quality in HILO illumination. **Right**: Workflow for nuclear segmentation in tkPAINT imaging. Data acquisition, localization and drift correction were performed as in a, only that individual localization clouds could serve as fiducials for drift correction and no gold particles were needed, similar to imaging DNA origami (1). Prior to each tkPAINT experiment, we acquired a single DAPI image for later nuclear segmentation. For each tkPAINT experiment, a corresponding binary mask was created out of the DAPI image analogously to a. We initially performed an affine transformation to match DAPI and 560 nm channel (Cy3b) using Fiji (7) for descriptor-based registration (8) based on TetraSpeck™ multicolor bead images, but found that the effect on the diffraction limited DAPI mask was negligible. Hence, a Python script was used to directly align DAPI masks and tkPAINT datasets, correcting for a potential lateral offset due to sample drift during the tkPAINT acquisition, and to subsequently filter for all nuclear localizations accordingly. **b**. tkPAINT Pol II S5p datasets acquired using standard imager sequence P1 and speed imager sequence R4. Interphase nuclei that entirely lied within the aligned DAPI mask after drift correction were selected. **c** HILO DNA-PAINT Pol II S5p datasets acquired using standard imager sequence P1 and speed imager sequence R4. **d** Localization precision (NeNA – Nearest Neighbor Analysis (11)) for tkPAINT and HILO datasets in b-c. **e** Signal-to-noise ratio for tkPAINT and HILO datasets in b-c. *n*=3 replicates per condition. Boxplots show the median (horizontal line), interquartile range (box limits) and whiskers extending to 1.5×IQR. Scale bars, 10 µm in (b).

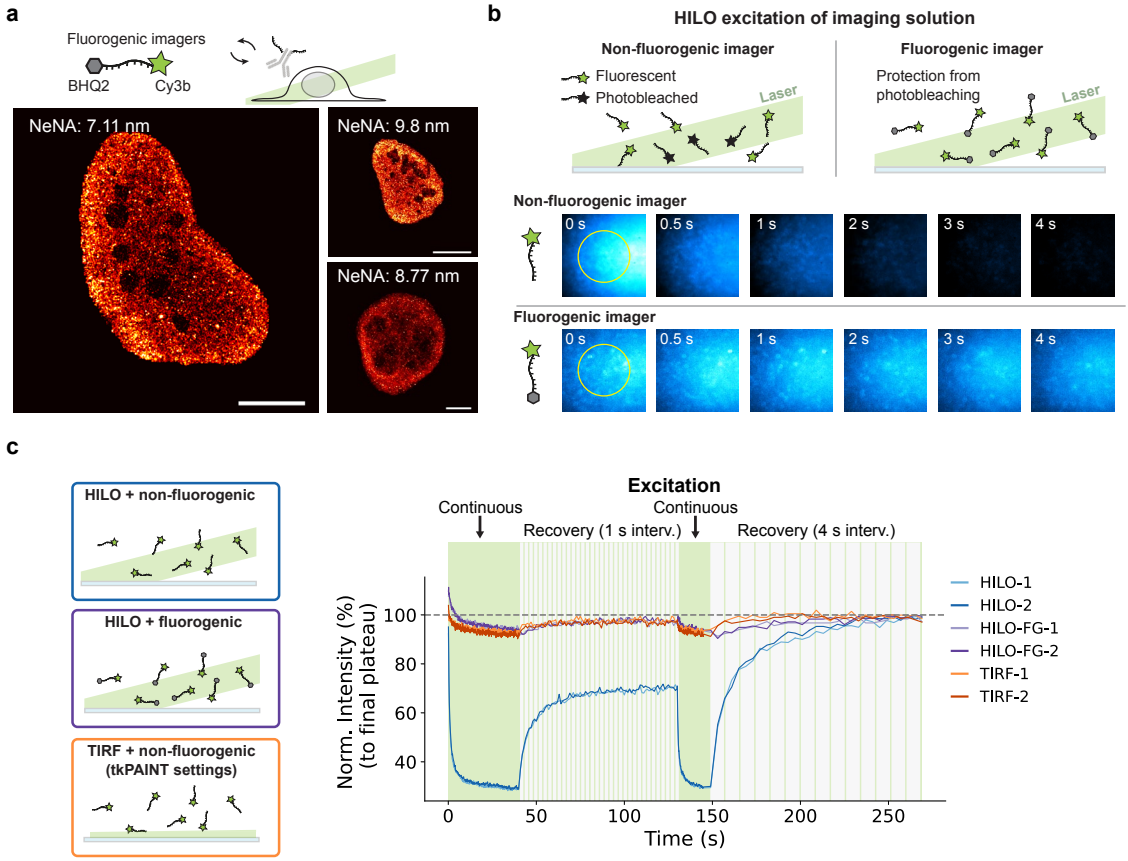

Fig. S3. tkPAINT does not require fluorogenic imagers for bleaching protection. a. HILO DNA-PAINT images of Pol II acquired using a fluorogenic imager design featuring a quencher molecule to suppress fluorescence of unbound imagers (12). The localization precision determined via NeNA is displayed for each dataset. **b**. Time series of imager bleaching upon HILO illumination. Fluorogenic imagers are protected from photobleaching in their unbound state during diffusion. **c** Fluorescence recovery after photobleaching experiment from the center circle as indicated by yellow circles in (b). First, the sample was continuously illuminated for 40 s and images acquired at 100 ms exposure time. Subsequently, fluorescence recovery was initiated by allowing 1 s intervals without excitation for 90 s. An additional 15 s period of bleaching was performed via full excitation before a second fluorescence recovery period was initiated allowing 4 s intervals without excitation for 120 s. Two independent repeats were performed for non-fluorogenic imager + HILO (blue), fluorogenic imager + HILO (purple) and non-fluorogenic imager + TIRF (the same acquisition settings as tkPAINT experiments; orange). Scale bars, 10 µm.

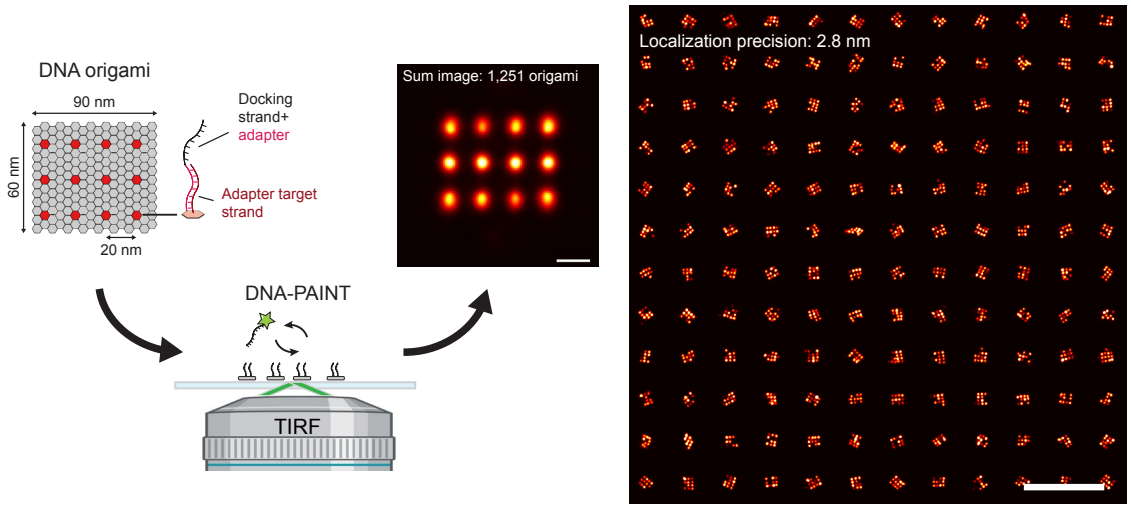

Fig. S4. TIRF-based DNA-PAINT imaging of synthetic DNA origami 20 nm grids. DNA-PAINT image of surface-immobilized DNA origami featuring a pattern of docking strands at 20-nm spacing ('20 nm grids' (1)) acquired on our TIRF system. The origami is designed in a modular fashion by carrying 12 anchored 20nt adapter target strands (dark red) to which docking strand-adapter hybrid oligos can be stably hybridized. This way the same origami structure can be used to test different imager-docking strand combinations (see **Methods**). The increased distance between docking strand and anchor point on the origami does not lead to a noticeable decrease in localization precision since the hybridized docking strand is still able to rapidly rotate around the anchor point such that on average emitted photons still allow to precisely pinpoint the anchor point(9). Note that for space reasons some origami illustrations within this work do not show the adapter explicitly, but this origami design was exclusively used for all DNA origami experiments shown. The left image displays an averaged sum image of 1,251 origami and the right image a random selection of 144 origami arranged in 12x12 square. The localization precision for the data set is stated in the right image. Scale bars, 20 nm in left image and 200 nm in right image.

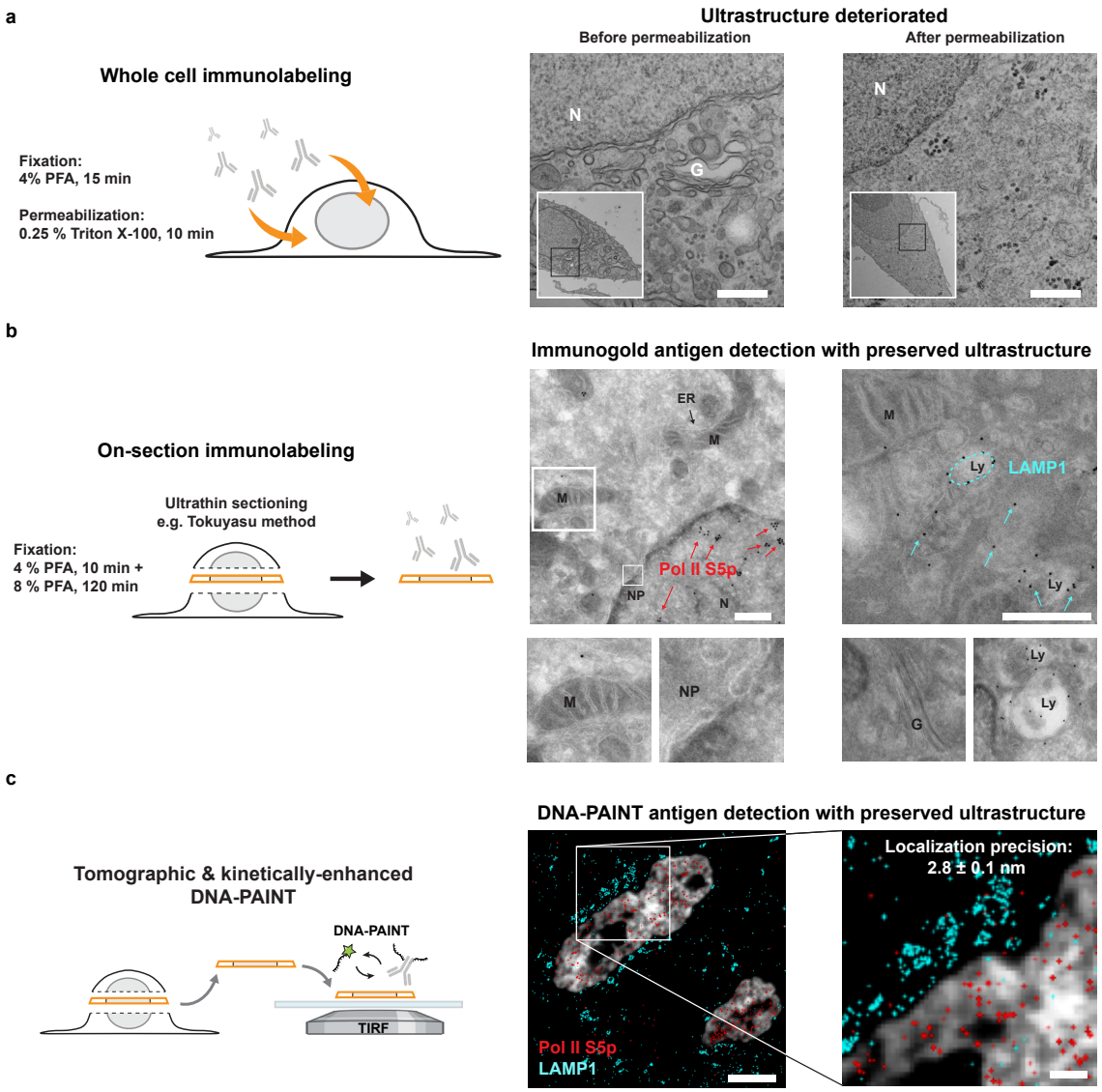

Fig. S5. tkPAINT enables cell-wide DNA-PAINT imaging under ultrastructure-preserved conditions at sub-3 nm localization precision. a Ultrastructural disruption in standard paraformaldehyde(PFA)-based immunofluorescence protocols for whole cells(13). Transmission electron microscopy (TEM) images of HeLa cells depict how brief fixation times lead to poor structural integrity and permeabilization with Triton X-100 causes reductions in cytoplasmic density as well as apparent organelle loss. Nuclear ultrastructure is relatively well-preserved even for brief fixation and permeabilization (Fig. S6). **b** Physical sectioning enables "on-section" labeling of intracellular antigens without permeabilization. TEM images show Tokuyasu cryosections of HeLa cells prepared following a PFA-based fixation protocol optimized for ultrastructural preservation. Immunogold reveals sites of cytoplasmic LAMP1 and nuclear Pol II S5p; Mitochondria (M), nuclear pores (NP), Endoplasmic Reticulum (ER). Golgi and lysosomes (Ly) are highlighted. **c** tkPAINT principle: physical sectioning (e.g. using the Tokuyasu method, same fixation conditions as in b) enables TIRF-based DNA-PAINT imaging of ultrastructurally-preserved specimens. Without permeabilization, immunolabeling occurs primarily at the section surfaces (14), while internal epitopes can be made accessible via brief permeabilization (see Fig. S6) without noticeable ultrastructural alteration inside the nucleus (see Fig. S1). The localization precision of 2.8 ± 0.1 nm was measured over four independent repeats (mean and std., respectively). Scale bars, 200 nm in (a), 400 nm in (b), 2 µm in (c) and 100 nm in zoom-in.

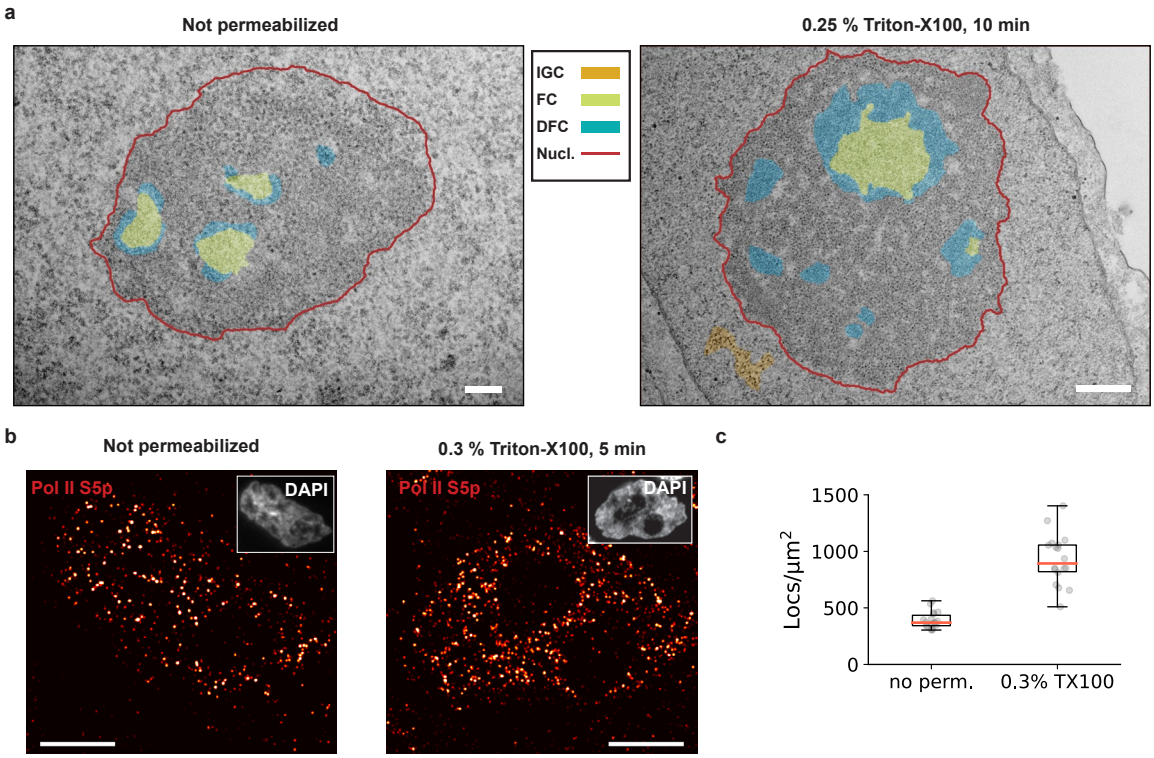

Fig. S6. Permeabilization enhances nuclear epitope accessibility without altering nuclear ultrastructure. a Annotated nuclear ultrastructure in TEM images shown in Extended Data Fig. 2a: 15 min fixation in 4 % PFA. No permeabilization (left image) vs. 10 min permeabilization in 0.25 % Triton X-100 (right image). Annotations: nucleolus (red line), dense fibrillar component (DFC, turquoise), fibrillar center (green) and interchromatin granular clusters (IGC; also nuclear speckles; yellow). Nuclear ultrastructure is relatively well-preserved even for such brief PFA fixation and permeabilization. **b** The Tokuyasu protocols developed by the Pombo lab (fixation: 4 % PFA for 10 min followed by 7 % PFA for 120 min) leverage brief permeabilizations with 0.2-0.3% Triton X-100 for 5-10 min (15, 16) to enhance epitope access for immunolabeling throughout the section volume. In Fig. S1 we validated via TEM that nuclear ultrastructure remains unaffected by this permeabilization step. Comparing tkPAINT images of Pol II S5p in non-permeabilized (left image) vs. permeabilized 150 nm-thin cryosections (0.3% Triton X-100 for 5 min; right image) visually confirmed increased labeling. The inset shows the DAPI channels of each nucleus. **c** Localizations per nuclear area measured for non-permeabilized vs. permeabilized tkPAINT datasets quantitatively confirming increased labeling. Due to higher antibody labeling, imager concentration in permeabilized tkPAINT datasets was half of that in non-permeabilized datasets and hence nuclear localization density was concentration adjusted. Boxplots show the median (horizontal line), interquartile range (box limits), whiskers extending to 1.5×IQR, and outliers (points beyond whiskers). One data set per condition; 3,479 vs. 8,051 localization clouds from each 18 cells (not-permeabilized vs. permeabilized sections, respectively. Boxplots show the median (horizontal line), interquartile range (box limits) and whiskers extending to 1.5×IQR. Scale bars, 200 nm and 600 nm in (a; left and right, respectively) and 3 µm in (b).

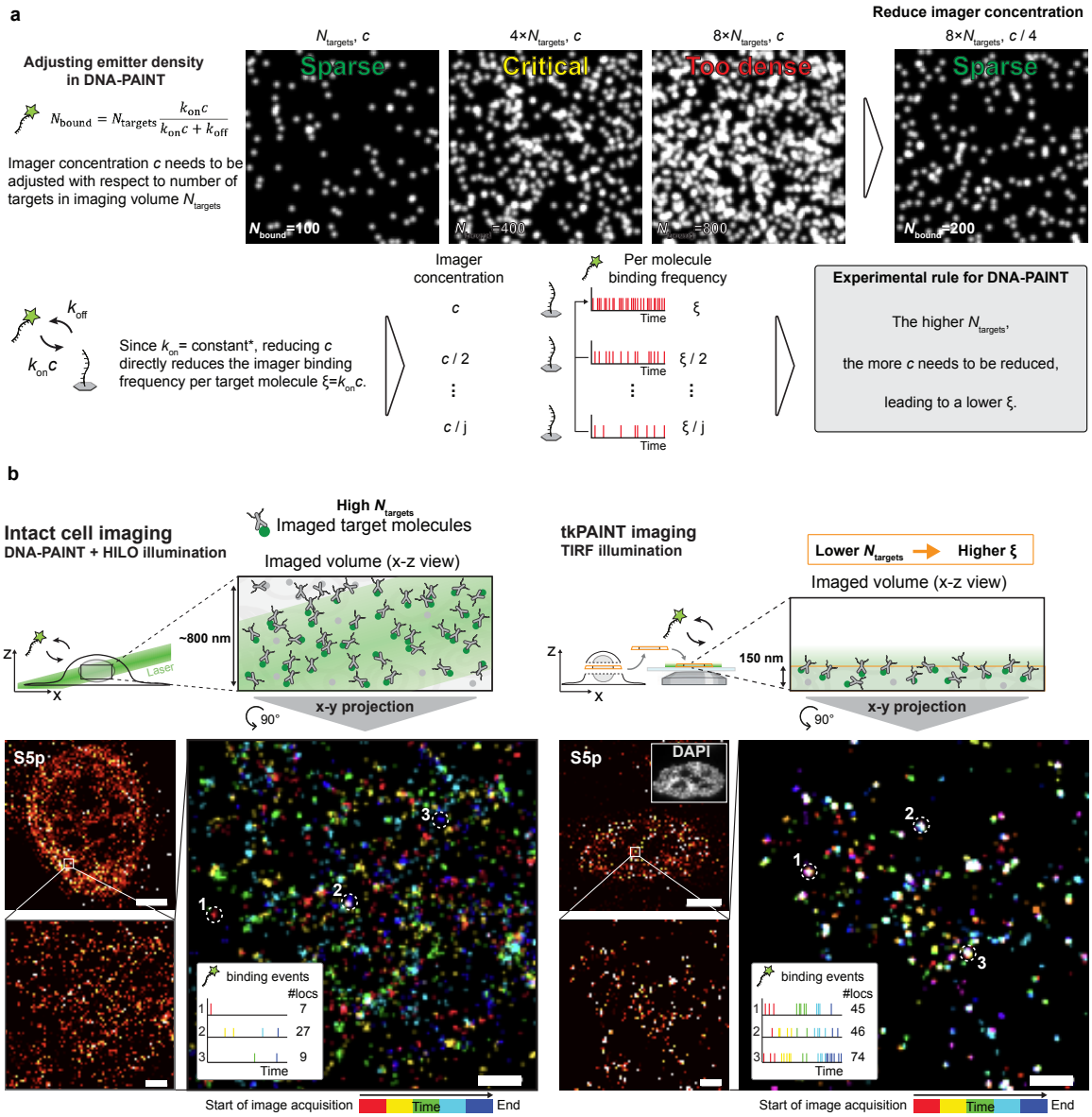

Fig. S7. Volume reduction in tkPAINT enhances per-molecule imager binding frequencies and shortens acquisition times. a Simulated raw DNA-PAINT images showcasing that the number of bound imagers at any given time, N_{bound}, must be low enough to ensure sparse single-molecule blinking required for SMLM reconstruction. $N_{\mathrm{bound}} = N_{\mathrm{targets}} \frac{k_{\mathrm{on}}c}{k_{\mathrm{on}}c+k_{\mathrm{off}}}$, where N_{targets} is the number of labeled target molecules within the imaging volume, k_{on} is the imager association rate, c the imager concentration and k_{off} is the imager dissociation rate. *Note that k_{on} and k_{off} of a given imager-docking strand pair are constant for set experimental conditions such as temperature and buffer conditions (17). For samples featuring a dense abundance of target molecules, N_{bound} can become too large and blinking events too dense, such that c needs to be reduced. However, a reduction in c inevitably leads to a decrease in the per-molecule imager binding frequency $\xi = k_{\mathrm{on}}c$. The number of randomly distributed emitters is stated in the bottom left corner of each simulated image and the image dimension are 16.64 µm x 16.64 µm. **b** Same HILO DNA-PAINT image and tkPAINT image as shown in **Fig. 1**c and d, respectively. Localizations in the zoom-in were color-coded according to registration time during data acquisition (five colors, e.g. red for first and blue for last temporal segment; total imaging time: ~17 min. The HILO DNA-PAINT image displays largely discretely colored localizations, which is expected since the large axial imaging volume in HILO bears a large N_{targets}, requiring to image at low imager binding frequency ξ that is not sufficient to repeatedly sample targeted molecules with imager binding events within the time of image acquisition. The tkPAINT image, in contrast, features concentrated accumulations of localizations of which many are revealed by temporal coloring as repetitive

'white-colored' localization clusters. The volume reduction in tkPAINT can thus be an effective way of enhancing imager binding statistics by reducing N_{targets} and thus allowing to image at higher per-molecule imager binding frequencies. For both images, time traces of imager binding and number of localizations are shown for three regions indicated by white circles, indicating high per molecule binding. This also directly implies that acquisition times can be reduced compared to whole cell imaging, since the same number of localizations per target molecule can be obtained in a shorter time compared to whole cell imaging. Scale bars, 5 µm in (**b**) and 400 nm in zoom-ins.

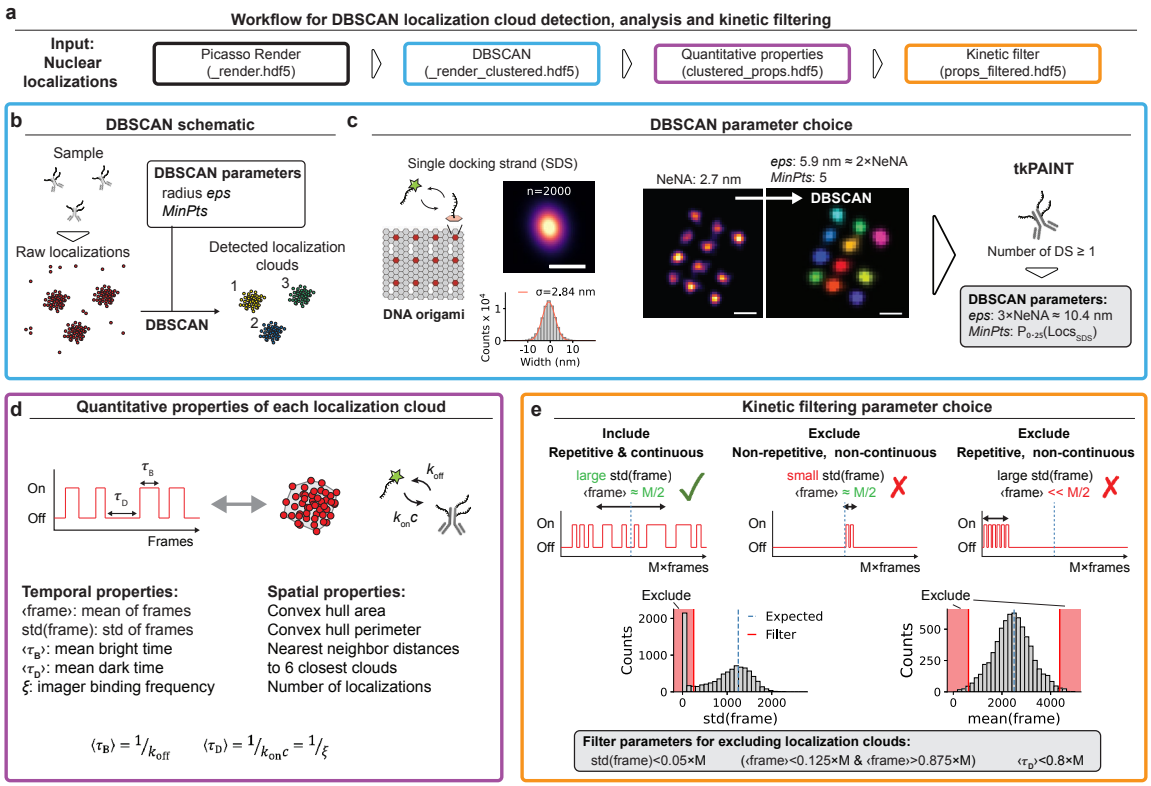

Fig. S8. DBSCAN localization cloud detection, quantitative analysis and kinetic filtering. a Overview of quantitative localization cloud analysis. Starting point of our spatiotemporal analysis were drift-corrected nuclear localizations (see **Fig. S2**). Subsequently the clustering algorithm DBSCAN was applied to identify localization clouds (blue box). For each localization cloud, its spatiotemporal quantitative properties were calculated (purple box). Finally, a kinetic filter was applied to remove non-repetitive localization clouds (orange box). **b** DBSCAN schematic. DBSCAN has two input parameters (18), *eps* (or epsilon; distance between points to be considered as within neighborhood) and *minPts* (number of points required to form a dense region). Both parameters must be chosen such that neighboring localization clouds are registered as single clouds. **c** DBSCAN parameter choice. In theory, the NeNA localization precision should correspond to the standard deviation σ of Gaussian distributed localizations from a single emitter (11) and has thus been suggested as input parameter for DBSCAN: *eps*=NeNA (19). We first validated the relation between the global NeNA value of a dataset and σ using DNA origami data acquired under tkPAINT conditions, where localizations from single emitters, i.e. single docking strands (SDSs) could be unambiguously identified. Indeed, NeNA and σ were in close agreement. However, since σ only contains ~68 % of Gaussian distributed data points, *eps* needs to be increased to capture also the outer localizations of a SDS localization cloud. On origami, we empirically found that adjusting *eps* to ~2xNeNA and *minPts* to 5 efficiently captured SDS localization clouds (colored SDSs on origami image indicate their identification as distinct clouds). In tkPAINT datasets, even a single primary antibody can yield overlapping localization clouds originating from more than one docking strand, because (i) an unknown number of docking strands is conjugated to each secondary antibodies or (ii) up to two nanobodies binding per primary antibody with one docking strand each. Since these localization clouds overlap, *eps* needs to be further increased. For tkPAINT we thus chose an average value corresponding to 3xNeNA as *eps* input. For *minPts* we chose the 25th percentile of the number localizations of localizations a SDS yielded on DNA origami imaged under identical conditions. **d** Calculation of quantitative spatiotemporal properties of each localization cloud. The left schematic shows a fluctuating intensity trace corresponding to a localization cloud with periods of imager binding ('on' or 'bright') and periods in between binding events without any localizations ('off' or 'dark'). The dwell times in each state are referred to as bright times τ_B and dark times τ_D, respectively, and allow for calculating imager association and dissociation rates (k_{on} and k_{off}, respectively) in DNA-PAINT (20) (see also **Extended Data Fig. 3** for a discussion on binding frequency ξ). Exploiting previously developed custom Python modules (picasso_addon (9), lbFCS (17) and lbFCS2 (3)), we calculated the stated temporal properties (⟨frame⟩, std(frame), $\langle\tau_B\rangle$, $\langle\tau_D\rangle$) and the number of localizations for each localization cloud. Using Scipy (21), we further computed the convex hull area, perimeter as well as the nearest neighbor distances to the six closest localization clouds. **e** Kinetic filtering parameter choice. **Top:** three schematic fluctuating intensity traces for a tkPAINT data acquisition of *M* frames are shown.

The left trace shows repetitive imager binding over the course of the experiment and thus has a mean frame ⟨frame⟩ value close to *M*/2 (dashed line). Due to many binding events, the standard deviation of frames is relatively large. Such a trace would fulfill the kinetic filtering criteria. In contrast, the center and right intensity traces correspond to exemplary localization clouds not fulfilling the kinetic filtering criteria and are thus removed prior to further analysis. Bottom: Distributions of ⟨frame⟩ and std(frame) for a tkPAINT dataset of 5,000 frames length (left and right, respectively). The red shaded areas indicate localization clouds that were excluded through kinetic filtering. The blue dashed lines indicate the expected value for ⟨frame⟩ (i.e. at 5,000/2=2,500 for this dataset) and std(frame) (i.e. at ≈5,000/4=1,250 for this dataset). The following kinetic filtering cut-offs were used: (⟨frame⟩<0.125×M & ⟨frame⟩>0.875×M) and std(frame)<0.05×M. Furthermore, localization clouds with a mean dark time $\langle \tau_D \rangle$ of longer than 80 % of the acquisition length (i.e. $\langle \tau_D \rangle$>0.8×M) were excluded.

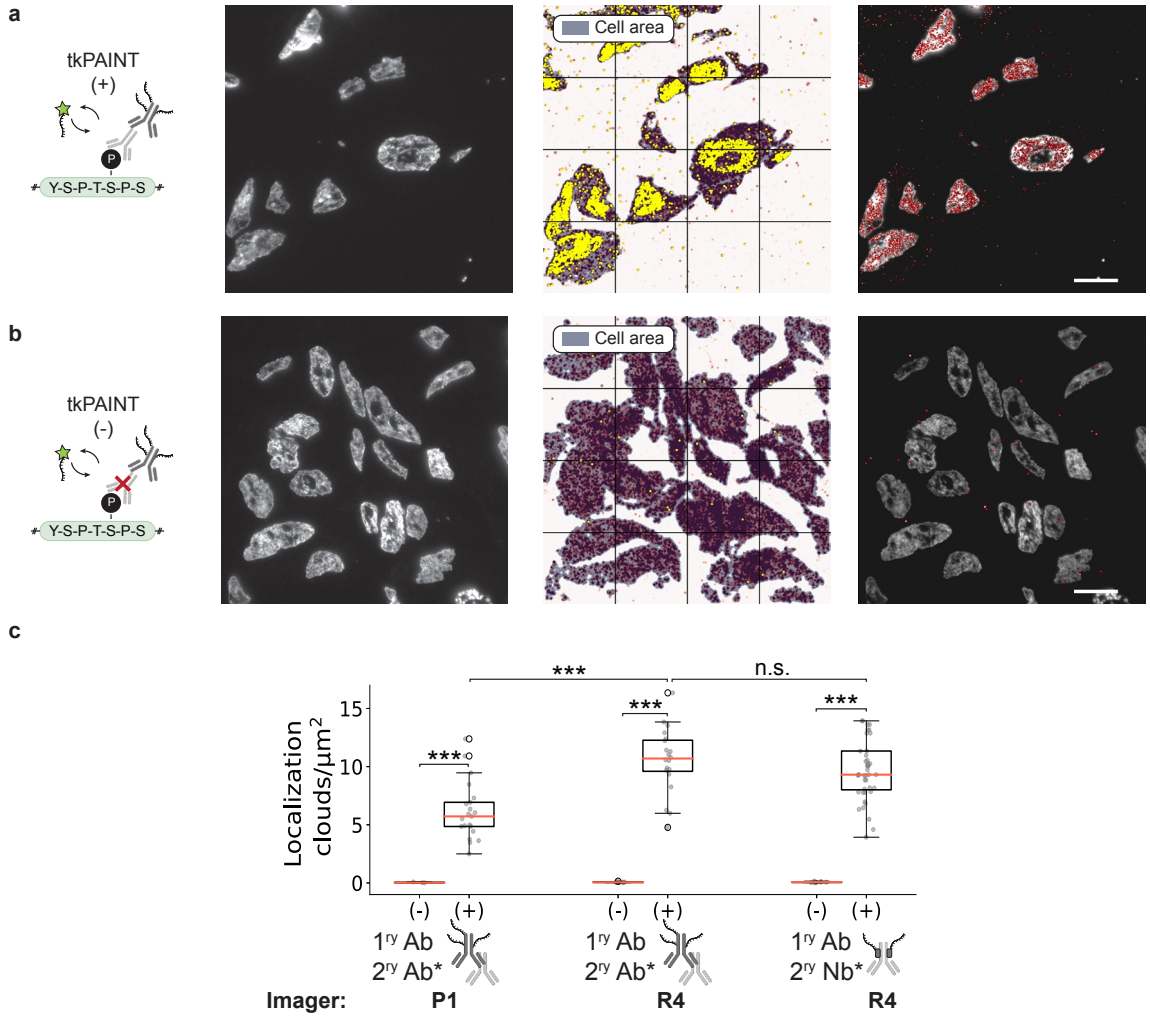

Fig. S9. Kinetic filtering efficiently removes non-repetitive localization clouds and allows quantitative evaluation of labeling strategies. a Exemplary tkPAINT Pol II S5p indirect immunolabeled (P1) dataset from **Fig. 2**a. Left: DAPI channel (left image). Middle: image containing all cellular localization clouds that passed kinetic filtering in yellow (both nuclear and cytoplasmic) overlayed over all recorded localizations marking the cellular area in blue. Right: All nuclear localization clouds that passed kinetic filtering (red). **b** Exemplary negative control tkPAINT dataset (P1) from **Fig. 2**c. Sample staining and imaging was performed as in a, but without addition of primary antibodies before incubation with DNA-conjugated secondary antibodies during sample preparation. Kinetic filtering efficiently excludes localization clouds that are not originating from primary antibodies. **c** Number of localization clouds per nuclear area for same imaging conditions as in **Fig. 2**b: (P1 – classic (1) vs. R4 – speed (22) using secondary antibodies) or comparing secondary labeling strategies (primary antibody (Ab) + secondary Ab (R4) vs. primary antibody + secondary nanobody (Nb)-R4). For each condition negative control (-) tkPAINT imaging was performed without the primary antibody but with the secondary label to assess the number of false positive localization clouds. False positives were negligible for all three cases (>140-fold difference between mean (+) and mean (-) for all three conditions). These tkPAINT datasets also allowed us to compare the detection efficiency between each labeling strategy, highlighting that secondary antibody-based tkPAINT imaging with speed imager R4 outperformed classic sequence P1, detecting 2× more nuclear Pol II S5p localization clouds (~12/µm^2 vs. ~6/µm^2, respectively). R4 in combination with secondary nanobodies yielded a similar density of nuclear localization clouds (~10/µm^2), demonstrating that secondary antibody-based amplification is not required for efficient primary antibody detection in tkPAINT. Two-sample t-test: ***p ≤ 0.001, n.s. (not significant) p > 0.05. *n*≥2 replicates per condition, each with ≥10 cells. Boxplots show the median (horizontal line), interquartile range (box limits) and whiskers extending to 1.5×IQR. Scale bars, 10 µm in (a,b).

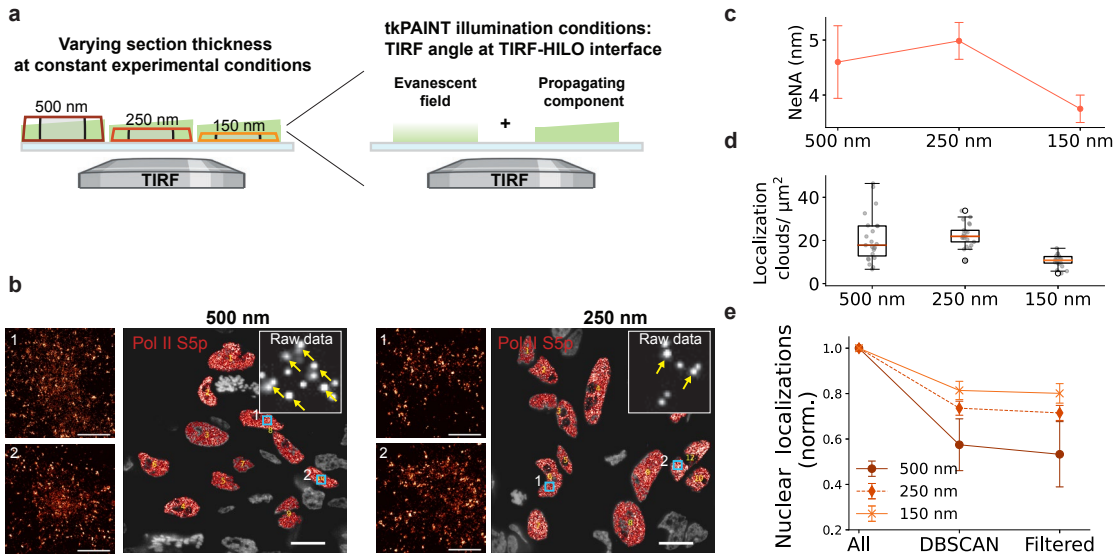

Fig. S10. Influence of section thickness on tkPAINT imaging. a Schematic illustrating tkPAINT imaging at three different cryosection thicknesses: 500 nm, 250 nm and 150 nm, as well as our illumination scheme. Note that under experimental conditions, TIRF is never perfect and in addition to the evanescent field that is exponentially decaying there is always a small fraction of laser light that propagates into the sample (e.g. due to finite beam divergence, glass surface roughness or refractive index inhomogeneities). By setting our TIRF angle just above the critical angle, we take advantage of this and ensure that we efficiently capture localizations throughout 150 nm sections, at relatively homogeneous illumination. The same illumination angle was used for thicker sections and proved sufficient to even illuminate a significant fraction of the 500 nm sections, although at decreasing intensity with increasing surface distance. **b** Exemplary tkPAINT S5p datasets shown for 500 nm and 250 nm cryosection thickness acquired under identical conditions as previous 150 nm thick cryosections (two datasets were acquired each). As expected from our discussion in Fig. S8, the zoom-ins show that tkPAINT images become more crowded, because with increasing thickness more antibodies are present within the imaged volume and thus populate the 2D super-resolved image. Since we applied the same imager concentration as for 150 nm sections, this led to a higher probability of simultaneous imager binding and hence overlapping blinking events in the raw data (see yellow arrows in inset and Fig. S8 for an explanation of this phenomenon). These “multi-emitter” events can still only be registered as a single localization and furthermore place the localization in between the actual emitter positions (2) (see more broadly spread localizations in between denser regions of antibodies in zoom-ins), which indicate that the imager concentration needs to be reduced. **c** NeNA localization precision decreases with cryosection thickness. Note that by adjusting the TIRF angle for minimal penetration depth, highest localization precisions should be achievable independent of section thickness (23). **d** Number of localization clouds per nuclear area vs. cryosection thickness showing a linear increase from 150 nm to 250 nm, but then saturates for 500 nm thick cryosections. **e** Kinetic filter yield shown for tkPAINT Pol II S5p 500 nm, 250 nm and 150 nm datasets. Normalized localization counts with respect to all initial nuclear localizations showing relative loss of localizations in each analysis step. *n*=2 replicates per condition, each with ≥5,800 localization clouds from ≥10 cells. Error bars in (c,e) correspond to mean and standard deviation. Boxplots in (d) show the median (horizontal line), interquartile range (box limits) and whiskers extending to 1.5×IQR. Scale bars, 10 µm.

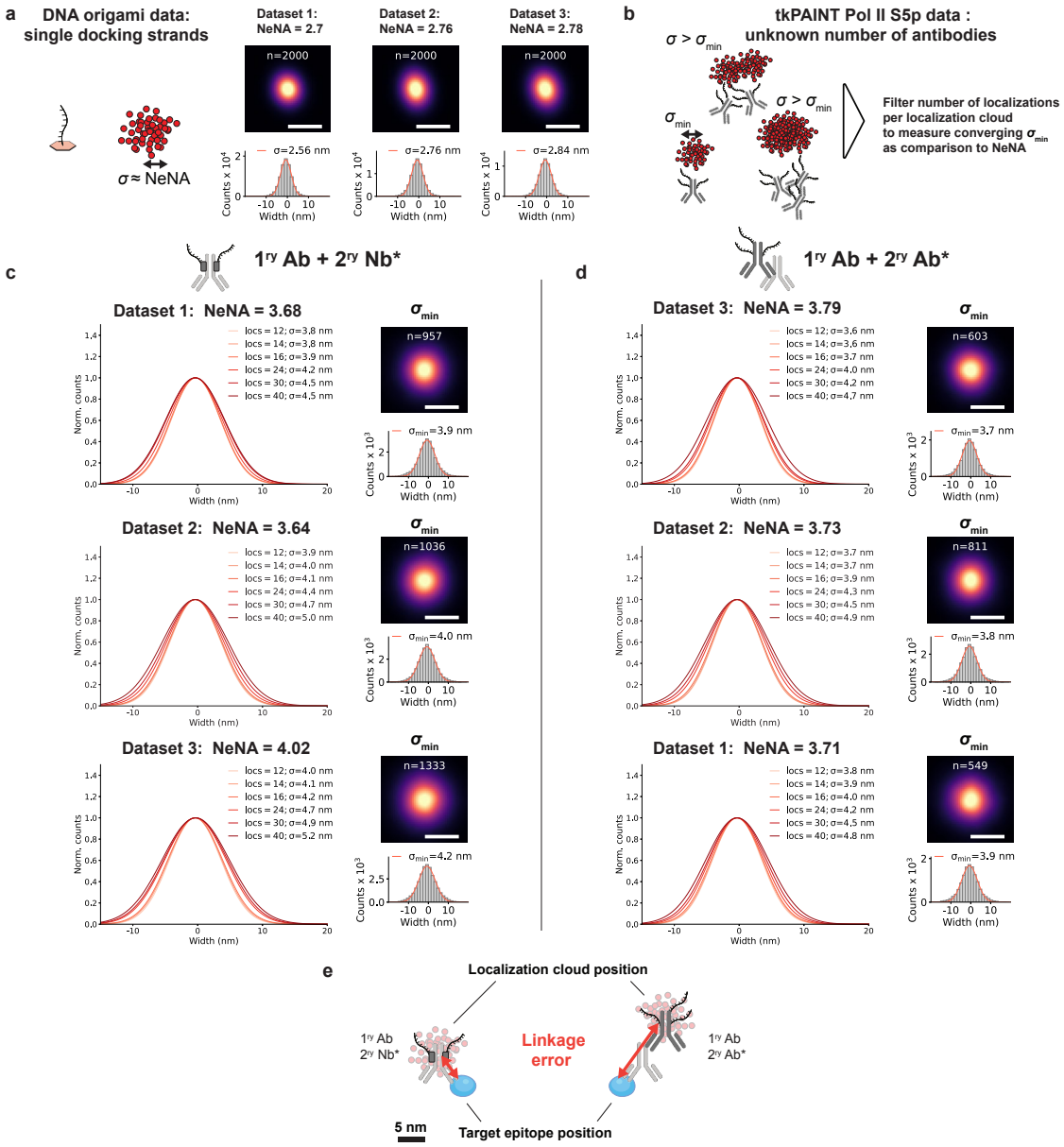

Fig. S11. Scan for convergent minimum number of localizations per cloud – HeLa cells. a Using DNA origami data acquired under identical conditions as tkPAINT experiments we measured the localization spread of single docking strands (SDSs). For each dataset we center-of-mass aligned 2,000 randomly-selected SDS localization clouds to obtain cloud average images (top). The histograms below show each localization distribution and a Gaussian fit (red curve) to obtain the standard deviation σ. The σ of Gaussian distributed SDS localizations is in relatively close agreement with the global NeNA localization precision (2.8 ± 0.1 nm and 2.7 ± 0.1 nm, respectively; mean ± standard deviation. See also Fig. S8). **b** In tkPAINT datasets, accumulations of antibodies with distances of only a few nanometers lead to enlarged localization clouds. We defined the standard deviation of the smallest localization clouds we could find as σ_{min} ("minimum" standard deviation) and hypothesized these correspond to single antibodies. To test this, we performed a range of center-of-mass alignments for localization clouds filtering for different maximum number of localizations to find σ_{min} as the converging standard deviation where further reduction in localization does not further reduce the localization spread. **c** Left: Range scan for maximum number of localizations per localization cloud for secondary nanobody-based tkPAINT Pol II S5p datasets to obtain the converging σ_{min}. Right: Localization distribution and Gaussian fit (red curve) for σ_{min} as well as averaged sum images above. The number of localization clouds per sum image is stated above. **d** Same as c but for secondary antibody-based tkPAINT Pol II S5p datasets. **e** Schematic of linkage error. Although it was not possible to observe resolution differences in secondary-nanobody labeled primary antibodies as compared to DNA-conjugated secondary antibodies

(σ_{min} of 4.0 ± 0.2 nm and 3.8 ± 0.1 nm, respectively; mean ± standard deviation), secondary nanobodies have the advantage of reducing the linkage error by which the physical size of the label displaces localization clouds away from the true epitope position. Observing similar σ_{min} can be explained by our range scan focusing on those secondary antibodies with only few docking strands, whereas for secondary nanobodies a maximum of two docking strands is present per primary antibody. Scale bars, 10 nm in averaged sum images.

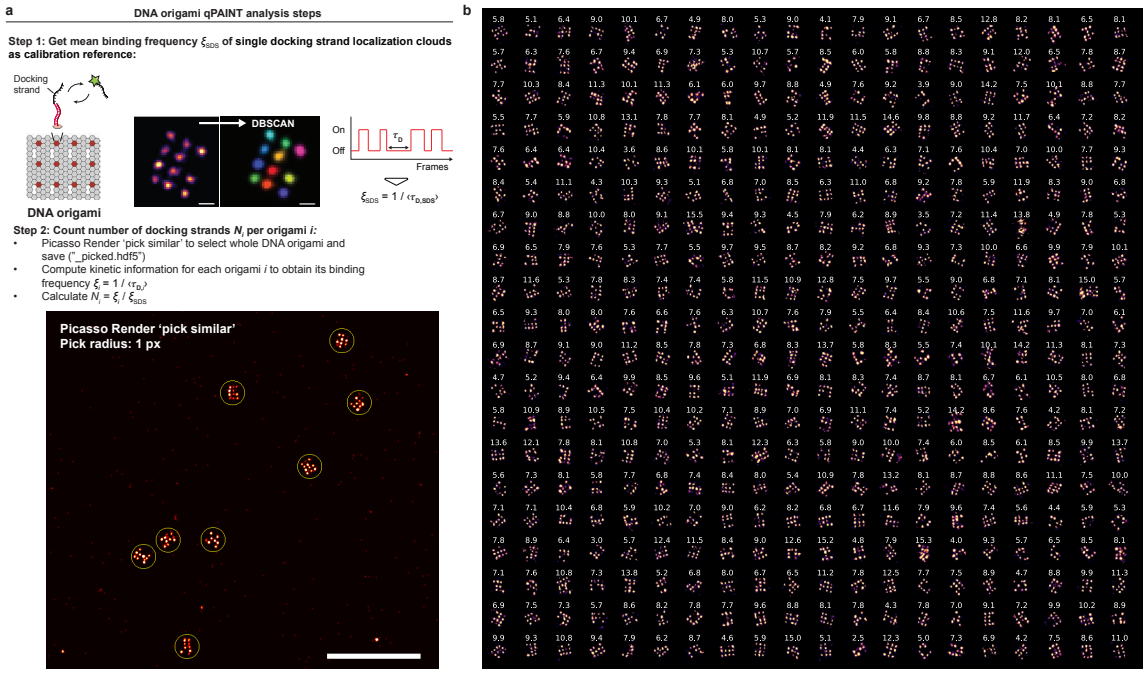

Fig. S12. qPAINT analysis steps for DNA origami data. a Analysis schematic for counting docking strands on DNA origami with qPAINT (24). The origami design (same as in Extended Data Fig. 1) features binding sites to which up to 12 docking strand-adapter oligos can be stably hybridized. In step 1, we applied DBSCAN to identify single docking strands (SDSs) on DNA origami and computed the average SDS binding frequency $\xi_{SDS} = 1/\langle \tau_{D,SDS} \rangle$ through measurement of the average dark times over all SDSs in the dataset. In step 2, we used Picasso Render(1) and its tool 'Pick Similar' to select entire DNA origami (yellow circles) and computed the binding frequency of each individual DNA origami ξ_i. The qPAINT counting result for each origami is then obtained via $N_i = \xi_i/\xi_{SDS}$. **b** 400 randomly selected DNA origami structures oriented as 20x20 grid. The qPAINT counting result is displayed above each origami. Scale bars, 500 nm in (b).

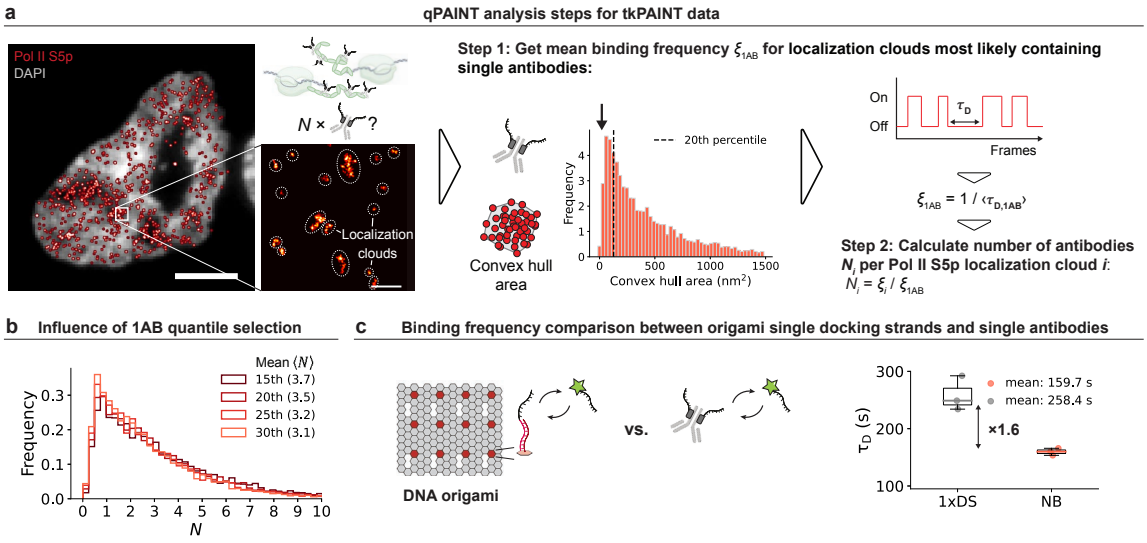

Fig. S13. qPAINT analysis steps for tkPAINT data. a Same Pol II S5p tkPAINT dataset as in Fig. 3a. Datasets featured sparse localization clouds from single antibodies and larger localization clouds containing several antibodies. In step 1 we defined a cut off at the 20th percentile of the convex hull area to define single antibody localization (1AB) clouds as qPAINT reference. For these, we calculated the reference binding frequency $\xi_{1AB} = 1/\langle \tau_{D,1AB} \rangle$ through measurement of the average dark times. In step 2, we obtained qPAINT antibody counting results for each localization cloud i in the dataset via $N_i = \xi_i/\xi_{SDS}$. **b** The influence of the convex hull area cut off choice on final counting results was minor. **c** Comparison of the mean dark time between single docking strands on DNA origami and single antibody localization clouds revealed 1.6-fold reduction, indicating 1.6 docking strands per primary antibody (note that only up to two nanobodies can bind one primary antibody and each nanobody carries one docking strand). *n*=3 replicates per condition. tkPAINT nanobody datasets each with ≥11,100 localization clouds from ≥10 cells. DNA-PAINT origami data sets each with ≥9,800 single docking strand localization clouds. Boxplots in (c) show the median (horizontal line), interquartile range (box limits) and whiskers extending to 1.5×IQR. Scale bars, 3 µm in (a) and 1 µm in zoom-in.

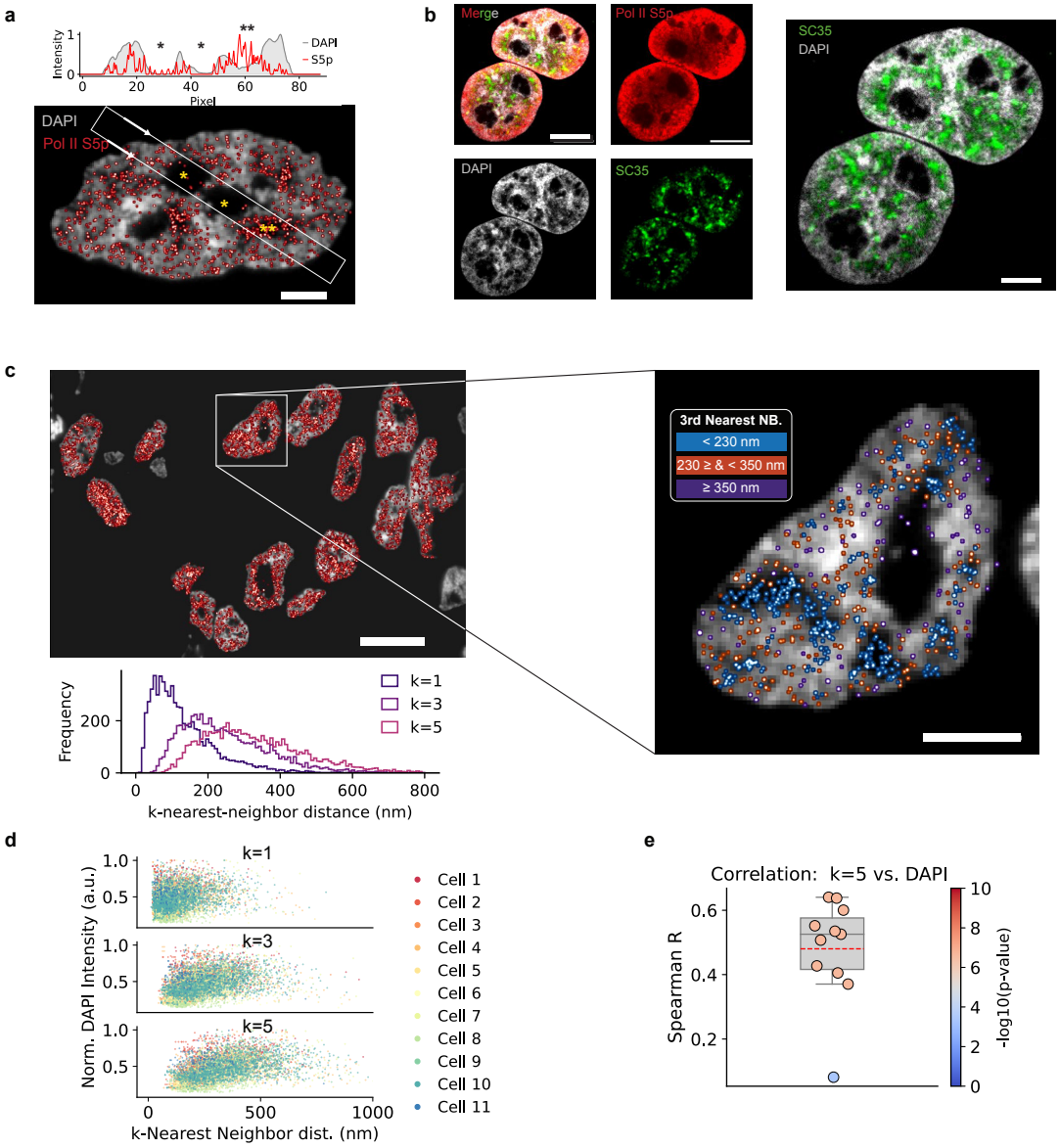

Fig. S14. Pol II S5p correlation analysis DAPI vs. nearest neighbor distances. a. Left: active Pol II associates with euchromatin featuring lower DAPI intensities compared to A-T rich and densely-packed heterochromatin. Center: Pol II S5p tkPAINT image including DAPI overlay (same as shown in **Fig. 2**a). Right: The line profiles below the image show the Pol II S5p and DAPI signal distribution across the white box indicated in the center image. The box first crosses two DAPI-weak regions without Pol II S5p signal followed by a third DAPI-weak region featuring high S5p signal. **b** To confirm the identity of DAPI-weak compartments containing Pol II S5p, we performed co-staining with the speckle marker SC35, showing that these regions correspond to nuclear speckles, as expected from literature (4). Fluorescence images were acquired in fixed whole HeLa cells using confocal microscopy. **c** Histogram of k-nearest-neighbor distances (k=1,3,5) between Pol II S5p localization clouds for the data set shown in **Fig. 3**a. In the magnified cell on the right localization clouds were colored according to their 3rd nearest neighbor distance (blue: <230 nm, red ≥ 230 nm & < 350 nm; purple ≥ 350 nm). The rendering visually confirms that DAPI-weak regions feature higher local abundances of Pol II S5p localization clouds (4, 25). Highly clustered Pol II (blue localization clouds) in DAPI weak areas likely correspond to nuclear speckles. **d** To quantify the anti-correlation between DAPI intensity (as a degree of chromatin compactness) and Pol II S5p abundance, we plotted k-nearest neighbor distances vs. normalized DAPI intensity for all nuclei in the data set. Indeed, localization clouds with small k-nearest neighbor distances, indicating a high local abundance of the antigen, were associated with DAPI weaker regions. The correlation becomes more pronounced for higher order nearest neighbor distances. **e** We calculated the Spearman rank-order correlation coefficient (R) for each cell in the data set (n=11) for the 5th nearest neighbor distance of

each localization cloud, confirming the correlation as highly significant ($R \approx 0.5$; $p < 0.0001$). A correlation of <1 is expected since Pol II is absent from nucleoli, which are also DAPI weak nuclear regions. tkPAINT nanobody dataset with 10,138 localization clouds from 11 cells. Boxplots in (c) show the median (horizontal line), mean (dashed horizontal line), interquartile range (box limits) and whiskers extending to 1.5×IQR. Scale bars, 10 μm in (b,c) and 3 μm in zoom in (c).

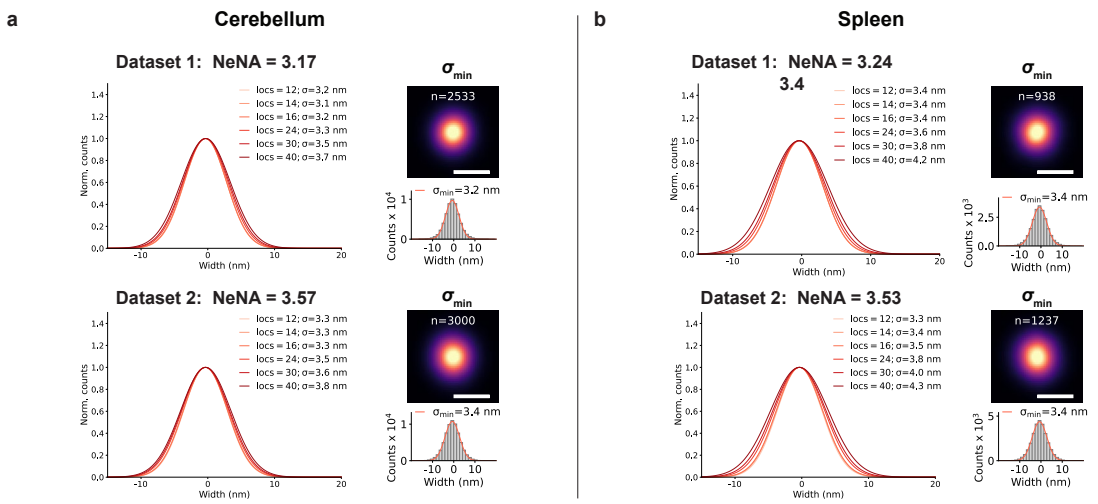

Fig. S15. Scan for convergent minimum number of localizations per cloud – mouse tissues. a This figure shows the same analysis introduced in Fig. S11 for HeLa cells, but for the mouse cerebellum datasets shown in Fig. 4. Left: Range scan for maximum number of localizations per localization cloud for secondary nanobody-based tkPAINT Pol II S5p datasets to obtain the converging σ_{min}. Right: Localization distribution and Gaussian fit (red curve) for σ_{min} as well as averaged sum images above. The number of localization clouds per sum image is stated above. **b** Same as a, but for mouse spleen datasets shown in Fig. 4. Scale bars, 5 nm.

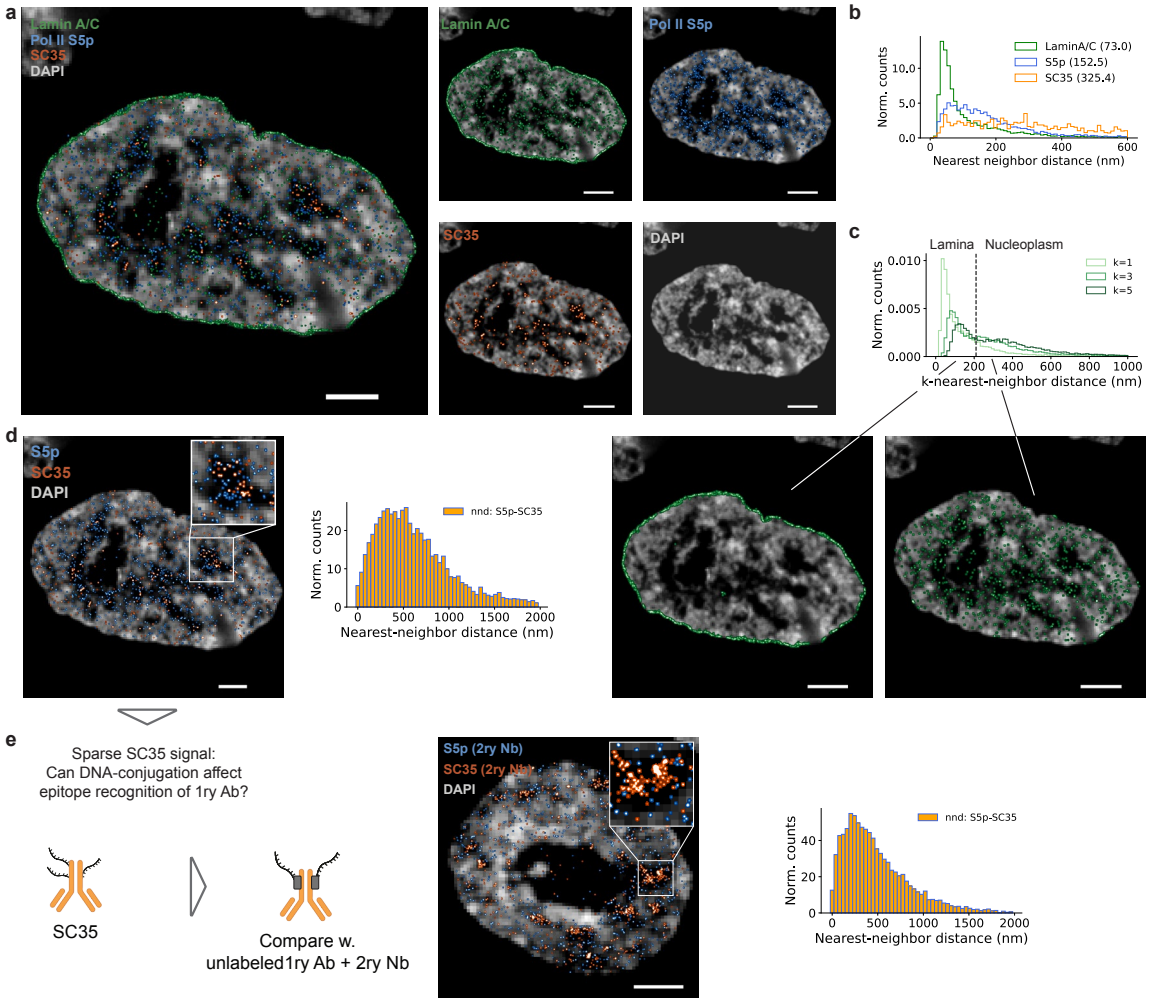

Fig. S16. Quantitative analysis of Exchange-tkPAINT for Lamin A/C, Pol II S5p, SC35 and primary antibody conjugation effects. a Exchange-tkPAINT image of Lamin A/C, Pol II S5p and SC35 including DAPI image (same as in **Fig. 4**a), overlayed on the left and displayed individually on the right. **b** Histogram of nearest neighbor distances measured individually for Lamin A/C, Pol II S5p and SC35. **c** Top: inspection of higher order nearest neighbor distance histograms revealed two peaks, indicating the lamina-associated fraction and the nucleoplasmic fraction of Lamin A/C, as confirmed when filtering for each peak (black dashed line) and visualizing the spatial distribution in the images below. **d** Intermolecular nearest neighbor distance measurements between Pol II S5p and SC35. The peak around 500 nm could indicates a spatial segregation, which has been similarly observed via genomics-based approaches (26). **e** Non-specific conjugation of primary antibodies with docking strands can affect antibody binding performance. Since SC35 signal was surprisingly sparse inside nuclear speckles, we repeated tkPAINT imaging using unconjugated SC35 antibodies plus secondary nanobodies. Obtaining much denser SC35 signal, we highlight the need to evaluate potential effects of DNA-conjugation on primary antibody performance for each target and recommend considering site-specific conjugation strategies (27) in future studies based on primary antibody DNA-PAINT/tkPAINT imaging. Overall, a similar Pol II S5p – SC35 nearest-neighbor distance pattern as in (d) was obtained. Scale bars, 3 μm.

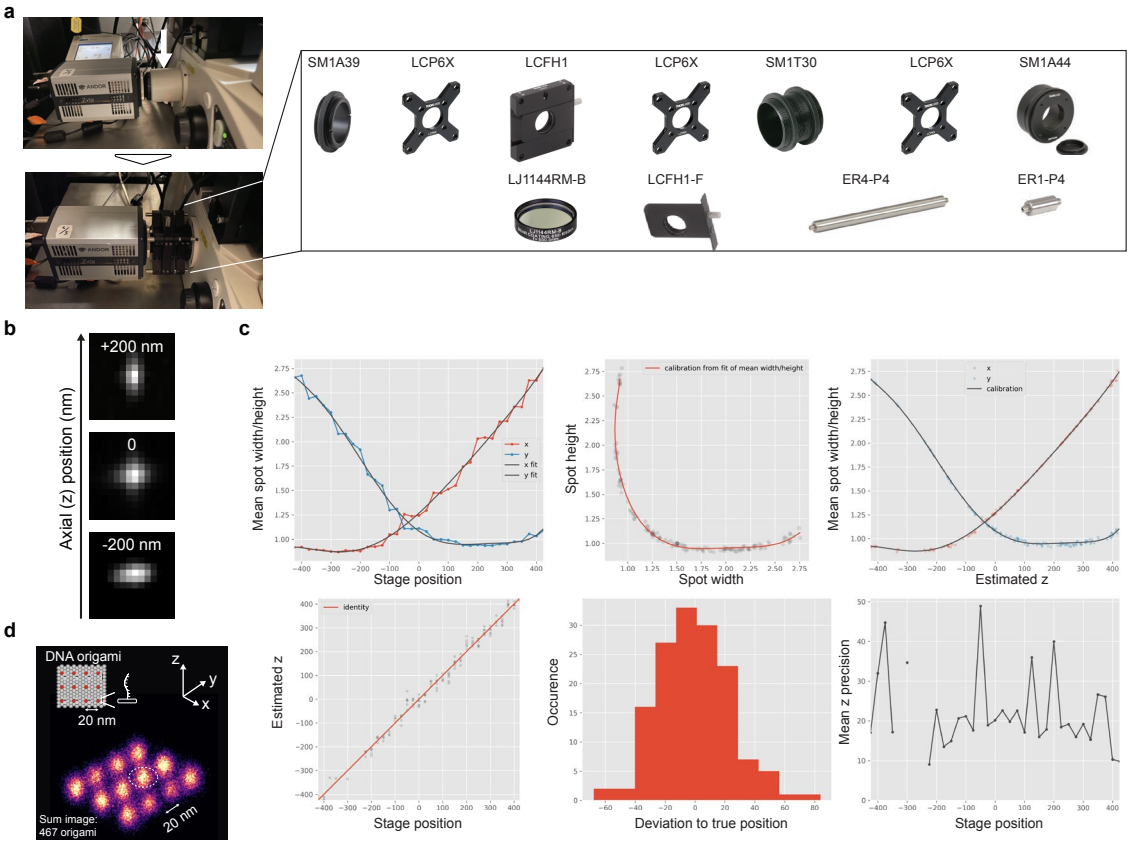

Fig. S17. Custom cylindrical lens insertion for 3D tkPAINT. a Parts list of Thorlabs optics components to replace the C-mount port (white arrow) at our standard Nikon TI Eclipse TIRF system with a cylindrical lens inset. Approximate cost at the time this manuscript was written: ~700 $. Part LCFH1-F can be purchased extra to leave an empty lens holder at the microscope for standard TIRF microscopy. The threaded tubing and our general design allow a flexible adjustment of the total distance between the camera and the port to match the focal length of the tube lens. **b** Axial calibration z-stack acquired using fluorescent beads. **c** Picasso Localize (1) output of 3D calibration: the z-stack was acquired at a step size of 25 nm and then loaded into Picasso Localize(1). Running “Calibrate 3D”, a box size large enough to fit the enlarged astigmatic point spread function was chosen. The generated 3D calibration .yaml file can be loaded when localization a 3D dataset, and the option “Fit z” needs to be ticket. Importantly, since insertion of an additional lens affects the magnification, this can be compensated for in Picasso. In our case, we determined the magnification factor by using DNA origami that carried a pre-designed 20 nm spacing as a nano ruler (**d**).

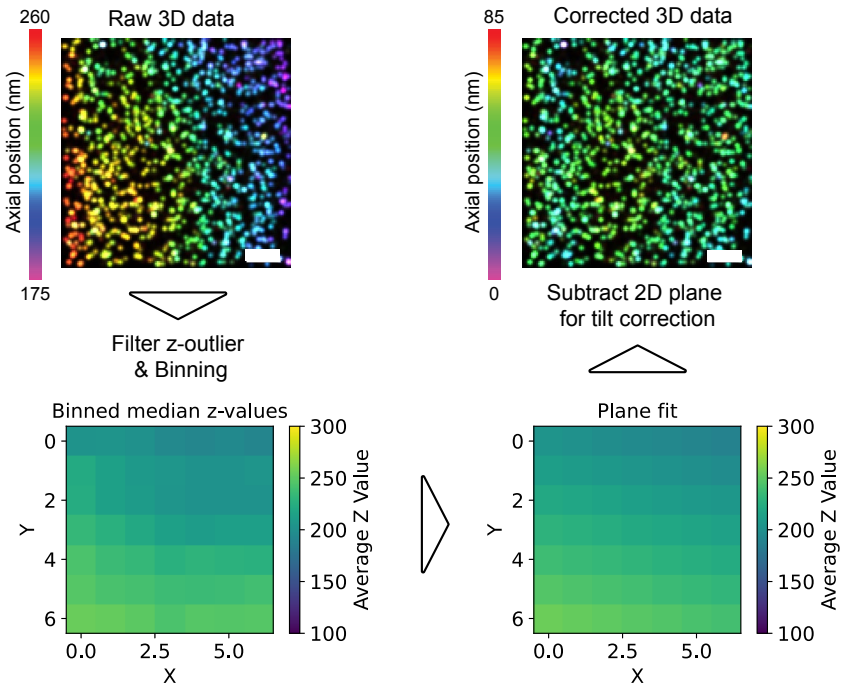

Fig. S18. Planar fit for axial tilt-correction in 3D tkPAINT. Axial tilt correction workflow shown at the example of a DNA origami 3D DNA-PAINT set using a custom Python implementation inspired by ref. (28). After removal of z-outliers (>4x median) the 3D dataset was binned into a pixelated map where each pixel was assigned the median z-position of all localizations within the pixel. Next a 2D plane was fit to the pixel map to approximate any tilt. Lastly, the planar fit was subtracted from the initial 3D tkPAINT dataset to remove axial tilt and normalize to z=0. Scale bars, 5 µm.

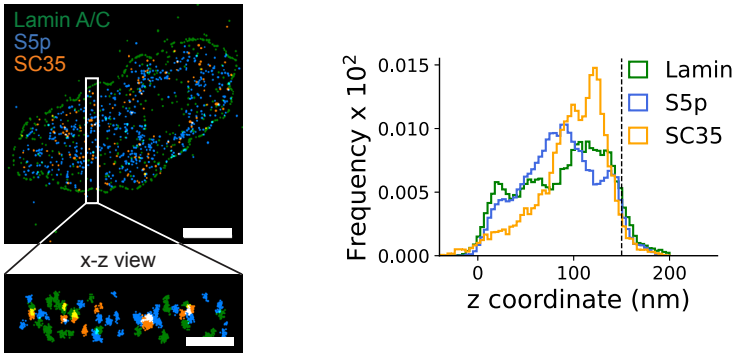

Fig. S19. Axial distribution of antibody signal for 3D Exchange-tkPAINT. Axial distribution of antibody signal for 3D Exchange-tkPAINT (Lamin A/C, POL II Pol II S5p and SC35) displayed in **Fig. 5**c. The dashed line indicates the set cutting thickness of 150 nm. Scale bars, 3 μm in (**a**) and 150 nm in zoom-in.

Table S1. Imaging parameters for tkPAINT/DNA-PAINT

Figure	No. datasets	Sample	Blocking buffer	Labeling (dilution, incubation time)	Imager	Imager conc. (pM)	Laser power objective (mW)	Exposure time (ms)	Frames	NeNA (nm)	Picasso DBSCAN MinLocs	Picasso DBSCAN epsilon (px)
HILO & tkPAINT P1												
1c, S2, S7	4	HeLa, whole cell	3% BSA + 0.25% Triton-X 100	1ry Ab: Rabbit Pol II S5p (1:200; overnight) + 2ry Ab: Donkey a-rabbit (1:200; 60min)	P1	~2000	~16	200	5,000	8.06 7.7 10.7 8.28	n.a.	n.a.
1d, 2a-b, S2, S7, S9	3	HeLa, cryosection (150 nm)	0.5% BSA + 0.2% gelatin 1% gelatin (2x)	1ry Ab: Rabbit Pol II S5p (1:200; 15min) + 2ry Ab: Donkey a-rabbit (1:200; 15min)	P1	~500	~16	200	5,000	2.98 3.48 2.93	10	0.08
HILO & tkPAINT R4												
S2	3	HeLa, whole cell	3% BSA + 0.25% Triton-X 100	1ry Ab: Rabbit Pol II S5p (1:200; overnight) + 2ry Ab: Donkey a-rabbit (1:200; 60min)	R4	~250	~16	100	9,000	8.35 6.34 9.27	n.a.	n.a.
S2, S7, S9	3	HeLa, cryosection (150 nm)	1% gelatin	1ry Ab: Rabbit Pol II S5p (1:200; 15min) + 2ry Ab: Donkey a-rabbit (1:200; 15min)	R4	~100	~16	100	9,000	3.81 4.05 4.21	10	0.08
HILO + fluorogenic imagers												
S3	3	HeLa, whole cell	3% BSA + 0.25% Triton-X 100	1ry Ab: Mouse Pol II S5p (1:200; overnight) + 2ry Ab: Goat a-mouse (1:200; 60min)	FP2	~1000	~16	100	9,000	7.11 9.8 8.77	n.a.	n.a.
Permeabilized vs. non-permeabilized tkPAINT												
S5, S6 (Exchange-PAINT LAMP1 & Pol II) (non-perm.)	2xP1 and 2x Pm2	HeLa, cryosection (150 nm)	1% gelatin	1ry Ab: Mouse Pol II S5p & Rabbit LAMP1 (both 1:200; 15min) + 2ry Ab: Donkey a-rabbit Pm2 & Goat a-mouse P1(both 1:200; 15min)	P1 Pm2	~1000 ~50	~16	200	5,000	P1: 2.7, 2.9 Pm2: 2.92, 2.74	10	0.08
S6 (perm.)	2	HeLa, cryosection (150 nm)	1% gelatin	1ry Ab: Mouse Pol II S5p + 2ry Ab: Donkey a-rabbit Pm2	P1 Pm2	~1000 ~50	~16	200	5,000	3.1 3.7	10	0.08
tkPAINT Pol II S5p 2ry nanobody & 2ry antibody comparison												
2b,e, 3a,c,d S9, S10, S11, S14	3	HeLa, cryosection (150 nm)	1% gelatin	1ry Ab: Rabbit Pol II S5p + 2ry Nb: Alpaca a-rabbit (both 1:200; pre-incubated for 20min in 20ul PBS, then filled with blocking buffer and incubated for 30min on sample)	R4	~100	~16	100	9,000	3.68 3.64 4.02	10	0.08
S11	3	HeLa, cryosection (150 nm)	1% gelatin	1ry Ab: Rabbit Pol II S5p (1:200; 15min) +2ry Ab: Donkey a-rabbit (1:200; 15min)	R4	~100	~16	100	9,000	3.793.733.71	10	0.08
tkPAINT negative controls												
2c, S9	2	HeLa, cryosection (150 nm)	1% gelatin	1ry Ab: - 2ry Ab: Donkey a-rabbit (1:200; 15min)	P1	~500	~16	200	5,000	3.29 4.28	10	0.08
S9	3	HeLa, cryosection (150 nm)	1% gelatin	1ry Ab: - 2ry Ab: Donkey a-rabbit (1:200; 15min)	R4	~100	~16	100	9,000	3.91 3.72 3.78	10	0.08
S9	3	HeLa, cryosection (150 nm)	1% gelatin	1ry Ab:- 2ry Nb: Alpaca a-rabbit (1:200; 30 min)	R4	~100	~16	100	9,000	3.72 3.81 3.51	10	0.08
PhosphatasePol II S5p IF controls												
2d, *phosphatase treated*	1	HeLa, cryosection (150 nm)	1% gelatin	1ry Ab: Rabbit Pol II S5p (1:200; 10min) + 2ry Ab: Donkey a-rabbit Alexa 488 (1:200; 10min)	n.a.	n.a.	n.a.	n.a.	n.a.	n.a.	n.a.	n.a.
2d, *not phosphatase treated*	1	HeLa, cryosection (150 nm)	1% gelatin	1ry Ab: Rabbit Pol II S5p (1:200; 10min) + 2ry Ab: Donkey a-rabbit Alexa 488 (1:200; 10min)	n.a.	n.a.	n.a.	n.a.	n.a.	n.a.	n.a.	n.a.

Cryosection thickness screen												
S10 (250 nm)	2	HeLa, cryosection (250 nm)	1% gelatin	1ry Ab: Rabbit Pol II S5p (1:200; 15min) + 2ry Ab: Donkey a-rabbit (1:200; 15min)	R4	~100	~16	100	9,000	5.96 4.74	10	0.1
S10 (500 nm)	2	HeLa, cryosection (250 nm)	1% gelatin	1ry Ab: Rabbit Pol II S5p (1:200; 15min) + 2ry Ab: Donkey a-rabbit (1:200; 15min)	R4	~100	~16	100	9,000	4.3 5.6	10	0.1
Mouse tissue tkPAINT												
4a-d, S11 (cerebellum)	2	HeLa, cryosection (150 nm)	1% gelatin	1ry Ab: Rabbit Pol II S5p + 2ry Nb: Alpaca a-rabbit (both 1:200; pre-incubated for 20min in 20ul PBS, then filled with blocking buffer and incubated for 30 min on sample)	R4	~100	~16	100	9,000	3.17 3.57	10	0.08
4a-d, S11 (spleen)	2	HeLa, cryosection (150 nm)	1% gelatin	1ry Ab: Rabbit Pol II S5p +2ry Nb: Alpaca a-rabbit (both 1:200; pre-incubated for 20min in 20ul PBS, then filled with blocking buffer and incubated for 30 min on sample)	R4	~100	~16	100	9,000	3.243 .53	10	0.08
Nuclear Exchange-tkPAINT, DNA, RNA												
5b, S16	1x R2 1xR3 1xR4	HeLa, cryosection (150 nm)	0.5% BSA + 0.2% gelatin	Mouse LaminA/C (R2) Rabbit Pol II S5p (R3) Mouse SC35 (R4) (all 1:200; overnight)	R2 R3 R4	~500 ~500 ~1000	~24	100	6,000	3.88 3.42 4.21	15	0.08
5c	1	HeLa, cryosection (150 nm)	3% BSA	Rabbit a-tubulin (1:200; overnight) Telomer FISH probe	P1	~100	~24	150	5,000	4.4	n.a.	n.a.
5d	1	HeLa, cryosection (150 nm)	1% gelatin	Poly(dT)-digoxigenin Mouse a-digoxigenin (1:100; 15 min) Goat a-mouse (1:100; 15 min)	P1	~500	~8	100	10,000	4.5	n.a.	n.a.
5g (3D)	1x R2 1xR3 1xR4	HeLa, cryosection (150 nm)	0.5% BSA + 0.2% gelatin	Mouse LaminA/C (R2) Rabbit Pol II S5p (R3) Mouse SC35 (R4) (all 1:200; overnight)	R2 R3 R4	~500 ~500 ~500	~24	100	6,000	5.7 5.03 5.57	n.a.	n.a.
DNA origami data												
3b, S5, S11a, S12, S13c	3	DNA origami, 20 nm grid	n.a.	n.a.	R4	~100	~16	100	9,000	2.7 2.77 2.78	5	0.05
S4	1	DNA origami, 20 nm grid	n.a.	n.a.	R3	~500	~16	100	9,000	2.8	n.a.	n.a.
5e-f, S17 (3D)	1	DNA origami, 20 nm grid	n.a.	n.a.	Pm2	~500	~16	100	6,000	3.99	n.a.	n.a.

Table S2. Used DNA-PAINT sequences

Imager-Docking ID	Docking sequence	Imager sequence
P1	ttATACATCTA	CTAGATGTAT-Cy3b
Pm2	ttCTCCTCCTCCTCCTCCTCCTCCTCCTCCTCC	GAGGAGG-Cy3b
R2	ttACCACCACCACCACCACCA	TGGTGGT-Cy3b
R3	ttCTCTCTCTCTCTCTCTCTC	GAGAGAG-Cy3b
R4	ttACACACACACACACACACA	TGTGTGT-Cy3b

SI References

1. J. Schnitzbauer, M. T. Strauss, T. Schlichthaerle, F. Schueder, R. Jungmann, Super-resolution microscopy with DNA-PAINT. *Nature Protocols* **12**, 1198 (2017).
2. F. Stehr, J. Stein, F. Schueder, P. Schwille, R. Jungmann, Flat-top TIRF illumination boosts DNA-PAINT imaging and quantification. *Nature Communications* **10**, 1268 (2019).
3. J. Stein, F. Stehr, R. Jungmann, P. Schwille, Calibration-free counting of low molecular copy numbers in single DNA-PAINT localization clusters. *Biophysical Reports* **1**, 100032 (2021).
4. S. Q. Xie, S. Martin, P. V. Guillot, D. L. Bentley, A. Pombo, Splicing Speckles Are Not Reservoirs of RNA Polymerase II, but Contain an Inactive Form, Phosphorylated on Serine2 Residues of the C-Terminal Domain. *Molecular Biology of the Cell* **17** (2006).
5. W. Möbius, G. Posthuma, Sugar and ice: Immunoelectron microscopy using cryosections according to the Tokuyasu method. *Tissue and Cell* **57**, 90–102 (2019).
6. G. Griffiths, *Fine Structure Immunocytochemistry* (Springer Berlin Heidelberg, 1993).
7. J. Schindelin, *et al.*, Fiji: an open-source platform for biological-image analysis. *Nat Methods* **9**, 676–682 (2012).
8. S. Preibisch, S. Saalfeld, J. Schindelin, P. Tomancak, Software for bead-based registration of selective plane illumination microscopy data. *Nat Methods* **7**, 418–419 (2010).
9. F. Stehr, *et al.*, Tracking single particles for hours via continuous DNA-mediated fluorophore exchange. *Nature Communications 2021 12:1* **12**, 1–8 (2021).
10. Y. Wang, *et al.*, Localization events-based sample drift correction for localization microscopy with redundant cross-correlation algorithm. *Opt. Express, OE* **22**, 15982–15991 (2014).
11. U. Endesfelder, S. Malkusch, F. Fricke, M. Heilemann, A simple method to estimate the average localization precision of a single-molecule localization microscopy experiment. *Histochemistry and Cell Biology* **141**, 629–638 (2014).
12. K. K. H Chung, *et al.*, Fluorogenic DNA-PAINT for faster, low-background super-resolution imaging. *Nature Methods* (2022). https://doi.org/10.1038/s41592-022-01464-9.
13. U. Schnell, F. Dijk, K. A. Sjollema, B. N. G. Giepmans, Immunolabeling artifacts and the need for live-cell imaging. *Nat Methods* **9**, 152–158 (2012).
14. Y.-D. Stierhof, H. Schwarz, H. Frank, Transverse sectioning of plastic-embedded immunolabeled cryosections: Morphology and permeability to protein A-colloidal gold complexes. *Journal of Ultrastructure and Molecular Structure Research* **97**, 187–196 (1986).
15. S. Q. Xie, L. M. Lavitas, A. Pombo, CryoFISH: fluorescence in situ hybridization on ultrathin cryosections. *Methods in molecular biology (Clifton, N.J.)* **659**, 219–230 (2010).
16. W. Winick-Ng, *et al.*, Cell-type specialization is encoded by specific chromatin topologies. *Nature 2021 599:7886* **599**, 684–691 (2021).
17. J. Stein, *et al.*, Toward Absolute Molecular Numbers in DNA-PAINT. *Nano Letters* **19**, 8182–8190 (2019).
18. M. Ester, H.-P. Kriegel, J. Sander, X. Xu, A Density-Based Algorithm for Discovering Clusters in Large Spatial Databases with Noise. *Proceedings of the 2nd International Conference on Knowledge Discovery and Data Mining* 226–231 (1996).
19. L. S. Fischer, *et al.*, Quantitative single-protein imaging reveals molecular complex formation of integrin, talin, and kindlin during cell adhesion. *Nat Commun* **12**, 919 (2021).
20. R. Jungmann, *et al.*, Single-Molecule Kinetics and Super-Resolution Microscopy by Fluorescence Imaging of Transient Binding on DNA Origami. *Nano Letters* **10**, 4756–4761 (2010).
21. P. Virtanen, *et al.*, SciPy 1.0: fundamental algorithms for scientific computing in Python. *Nat Methods* **17**, 261–272 (2020).
22. S. Strauss, R. Jungmann, Up to 100-fold speed-up and multiplexing in optimized DNA-PAINT. *Nature Methods* **17**, 1–3 (2020).
23. K. K. Narayanasamy, *et al.*, Visualizing Synaptic Multi-Protein Patterns of Neuronal Tissue With DNA-Assisted Single-Molecule Localization Microscopy. *Frontiers in Synaptic Neuroscience* **13** (2021).
24. R. Jungmann, *et al.*, Quantitative super-resolution imaging with qPAINT. *Nat Methods* **13**, 439–442 (2016).
25. P. V. Guillot, S. Q. Xie, M. Hollinshead, A. Pombo, Fixation-induced redistribution of hyperphosphorylated RNA polymerase II in the nucleus of human cells. *Experimental Cell Research* **295**, 460–468 (2004).
26. Y. Chen, *et al.*, Mapping 3D genome organization relative to nuclear compartments using TSA-Seq as a cytological ruler. *Journal of Cell Biology* **217**, 4025–4048 (2018).
27. J. Hellmeier, *et al.*, Quantification of absolute labeling efficiency at the single-protein level. *Nat Methods* 1–6 (2024). https://doi.org/10.1038/s41592-024-02242-5.
28. C. Franke, *et al.*, Approach to map nanotopography of cell surface receptors. *Commun Biol* **5**, 1–16 (2022).